Aksaray University
Journal of Science and Engineering

e-ISSN: 2587-1277
http://asujse.aksaray.edu.tr

Aksaray J. Sci. Eng.
Volume **10**, Issue **1**, pp. **32-58.**

Available online at DergiPark AKADEMİK

Research Article

Multi-Class Brain Tumor MRI Classification Using MS-GHOST-RAAE on a Combined Figshare-Br35H-SARTAJ Dataset

Cemal Yılmaz[1], Çağrı Suiçmez[1,2*], Alihan Suiçmez[3], Mehmet Fatih Işık[4]

[1]*Gazi University, Faculty of Technology, Department of Electrical and Electronics Engineering, Ankara, Türkiye.*
[2]*Gazi University, Graduate School of Natural and Applied Sciences, Ankara, Türkiye.*
[3]*Amasya University, Faculty of Engineering, Department of Electrical and Electronics Engineering, Amasya, Türkiye.*
[4]*Hitit University, Faculty of Engineering, Department of Electrical and Electronics Engineering, Çorum, Türkiye.*

Keywords
Brain tumor classification, Deep learning, MS-GHOST-RAAE, Machine learning, Wavelet transformation, MRI

Article information
Received: May 12, 2026
Revised: May 20, 2026
Accepted: May 20, 2026
Online: Jun 4, 2026

İz: **izlik.org/JA85GU54YW**
doi: **10.29002/asujse.1950042**

Abstract

This study proposes a hybrid deep learning framework for multi-class brain tumor classification using a combined MRI dataset constructed from Figshare, Br35H, and SARTAJ sources. The dataset includes 7023 MRI images belonging to four clinically important classes: glioma, meningioma, no-tumor, and pituitary tumor. In the proposed approach, a dedicated preprocessing pipeline is first applied to enhance tumor-related image regions and reduce irrelevant background information. Then, the Multi-scale GHOST Residual Attention Autoencoder (MS-GHOST-RAAE) is used for deep feature extraction. This architecture integrates multi-scale GHOST modules, residual connections, and attention mechanisms to obtain compact, stable, and discriminative feature representations. The extracted features are subsequently classified using conventional machine learning classifiers. Experimental results show that the proposed hybrid framework achieves 98.75% accuracy on the combined dataset, with a total processing time of 543 + 269.4571 s. These findings indicate that MS-GHOST-RAAE provides strong classification performance on heterogeneous MRI images and offers an effective computer-aided decision-support approach for brain tumor classification.

1. Introduction

The human brain is among the most important organs in the body due to its fundamental functions such as managing motor skills, performing cognitive functions, interpreting sensory stimuli, and controlling vital physiological processes. In this context, abnormal formations such as brain tumors can cause serious impairments in neurological functions; and if not detected early and accurately, they can lead to life-threatening clinical consequences [1,2]. The most common intracranial tumors are glioma, meningioma, and pituitary tumors. Accurately differentiating these tumor types is crucial. Correct identification of non-tumor images is also essential. This is important for diagnosis, treatment planning, surgical decisions, and patient follow-up. Magnetic resonance imaging (MRI) and computed tomography (CT) scans are commonly used to detect and evaluate brain tumors [3,4]. Because it offers precise information about the structure of the brain and makes soft tissues more visible, magnetic resonance imaging (MRI) is a commonly utilized approach in brain tumor analysis. However, analyzing MRI pictures by hand takes time and relies on the expertise of the professional. Different radiologists may interpret the same image differently, which could have an impact on the diagnosis. Computer-aided systems have therefore become more significant. These machine learning and deep learning-based algorithms are used to automatically identify and categorize brain cancers [5-7]. Three fundamental steps make up traditional procedures. The image is preprocessed first. Important features are then taken out of the picture. Classification is carried out at the last phase. Previous research has employed a variety of techniques. These include of segmentation, thresholding, edge enhancement, and median filtering. These techniques are employed to improve the visibility of the tumor area. Additionally, they aid in lowering image noise [8-13]. Additionally, techniques based on artificial intelligence have been created. These techniques are applied to classification and segmentation. Reducing the need to manually define tumor boundaries is the goal. Additionally, it lessens the need for professional interpretation [14-18]. These conventional techniques are capable of extracting valuable features. Nevertheless, these features are created by hand. As a result, a number of factors affect how well these approaches work. First, segmentation needs to be done correctly. Second, the tumor structure must be accurately represented by the manually extracted features. It can be difficult to depict intricate tumor patterns. As a result, the effectiveness of conventional approaches might be restricted.

Deep learning has led to significant advancements in medical image analysis thanks to its ability to directly and automatically learn hierarchical and distinctive features from image data [19,20]. Convolutional neural networks (CNNs), in particular, have become prominent models in image classification due to their ability to capture local spatial patterns,

[*] ***Corresponding Author:*** ▪cagrisuicmez@gazi.edu.tr 0000-0002-9709-2276

Articles in this journal is licensed under a Creative Commons Attribution-ShareAlike 4.0 International License.

edge information, texture features, and higher-level semantic representations [21,22]. Widely known CNN architectures such as AlexNet, VGGNet, GoogleNet, ResNet, DenseNet, and their derivatives have been successfully implemented in brain tumor classification tasks [23,24]. In addition, hybrid models that combine deep feature extraction with traditional machine learning classifiers such as support vector machines, decision trees, random forests, K-nearest neighbors, and Naive Bayes have also shown promising classification performances [25,26].

Some issues still exist in spite of these developments. It is possible to obtain MRI pictures from many data sources and facilities. The contrast, resolution, and imaging circumstances of these photographs could vary. Additionally, different images may show different anatomical features in the brain. As a result, models that were trained using just one dataset might not be adequate. It's possible that these models don't accurately reflect actual clinical settings. Additionally, the implementation of very deep transfer learning models in a clinical setting may be challenging due to their high processing power and memory requirements. Achieving high classification accuracy and doing well in feature extraction are also crucial. Low computational expenses must be maintained at the same time. It's still quite difficult to balance these three factors.

This work proposes a hybrid brain tumor MRI classification technique to solve these problems. This technique combines conventional machine learning classifiers with the MS-GHOST-RAAE model. Instead of using distinct datasets, the study focuses on a merged MRI dataset. The Figshare, Br35H, and SARTAJ sources were used to create this dataset. Four classes are included in the combined dataset: meningioma, glioma, no-tumor, and pituitary tumor. The dataset is more diverse due to the use of photos from many sources. As a result, the proposed approach was evaluated in a more difficult classification setting. This setting is also more similar to actual clinical settings.

The use of a multi-source heterogeneous MRI dataset is an important aspect of this study. MRI images collected from different data sources may have different contrast levels, resolutions, noise characteristics, and tumor appearances. Therefore, a model evaluated on only one dataset may not fully reflect real clinical variability. In this study, the combined Figshare–Br35H–SARTAJ dataset provides a more diverse and challenging evaluation environment. This allows the proposed MS-GHOST-RAAE framework to be tested under more realistic multi-class brain tumor classification conditions.

First, there is a unique preprocessing step in the proposed method. Tumor-related areas are made more noticeable with this phase. Grayscale transformation, binary thresholding, Otsu thresholding, region of interest extraction, color-based segmentation, masking, blurring, Canny edge detection, contour detection, and wavelet transformation are some of the preprocessing techniques. These steps are primarily intended to eliminate superfluous background information and emphasize tumor locations prior to feature extraction. The MS-GHOST-RAAE architecture is then employed. Short and unique deep characteristics are extracted by this architecture. While maintaining crucial spatial information, the multi-scale GHOST module aids in lowering computing load.

The connections now improve the gradient flow, allowing for more stable model training. The attention mechanism helps the model focus on key tumor-related features. In the final stage, the extracted deep features are classified using various machine learning methods, including RF, SVM, NB, DT, KNN, LR, MLP, GBC, ABC, and clustering-based classifiers.

Results from experiments have demonstrated the effectiveness of the proposed hybrid approach. In the combined Figshare–Br35H–SARTAJ dataset, the method's accuracy rate was 98.75%. 543 + 269.4571 seconds was the total processing time. These outcomes show how reliable MS-GHOST-RAAE-based feature extraction is. The technique is capable of successfully differentiating between MRI pictures from various sources. It also provides a workable structure in terms of processing time. This outcome is further supported by comparisons with models based on transfer learning. Results from experiments have demonstrated the effectiveness of the proposed hybrid approach.

The main contributions of this study are summarized as follows:

- A hybrid brain tumor MRI classification framework is proposed by integrating custom preprocessing, MS-GHOST-RAAE-based deep feature extraction, and traditional machine learning classifiers.
- The proposed method was evaluated on a heterogeneous combined MRI dataset containing glioma, meningioma, non-tumor, and pituitary tumor classes generated from Figshare, Br35H, and SARTAJ sources.
- The MS-GHOST-RAAE architecture combines multi-scale GHOST modules, residual connections, and attention mechanisms to produce compact and distinctive feature representations with reduced computational iteration.
- Multiple machine learning classifiers were used to evaluate the transferred deep features, thus providing a comprehensive assessment of the hybrid classification strategy.
- The proposed framework demonstrated strong performance on the combined multi-source MRI dataset, achieving 98.75% classification accuracy with a total processing time of 543 + 269.4571 seconds.

The remaining sections of the article are organized as follows. Section 2 examines studies related to brain tumor MRI classification. Section 3 describes the proposed method. This section explains the preprocessing steps, the MS-GHOST-RAAE architecture, feature extraction, and machine learning-based classification. Section 4 presents the experimental

results obtained on the combined dataset. Ablation analyses and comparative evaluations are also presented. Finally, Section 5 concludes the study and provides information about potential future research.

2. Literature Survey

Brain tumor classification from magnetic resonance imaging (MRI) data has been extensively investigated using classical machine learning, deep learning, transfer learning, attention mechanism models, and hybrid learning approaches. However, a significant portion of current studies evaluate their models on single-source datasets such as Figshare, SARTAJ, BraTS, Kaggle-based data collections or custom MRI datasets. While these studies make significant contributions to the literature, single-source evaluations may be insufficient to fully represent the heterogeneous structure in MRI images obtained from different data repositories.

Since the present study focuses only on the combined Figshare + Br35H + SARTAJ dataset, the literature comparison was reorganized accordingly. Therefore, Table 1 includes only studies that used the same combined dataset structure. This allows a more objective comparison between the proposed method and previous work under a similar multi-source and multiclass MRI classification setting.

Table 1. Studies using the combined Figshare + Br35H + SARTAJ dataset

References	Image Pre-processing	Classification	Dataset	Accuracy (%)	Classification Type
[27]	No	DT, NB, KNN, SVM	Including Figshare + Br35H + SARTAJ	0.9793	Multiclass
Proposed Method	**Grayscale conversion, Otsu thresholding, ROI extraction, color segmentation, masking, Canny edge detection, contour detection, and wavelet transformation**	**ML classifiers**	**Combined Figshare + Br35H + SARTAJ dataset**	**0.9875**	**Multiclass**

As shown in Table 1, the study in Celik and Inik (2024) [27]. used the combined Figshare + Br35H + SARTAJ dataset and achieved 97.93% accuracy using CNN-based feature extraction with conventional machine learning classifiers such as DT, NB, KNN, and SVM. This study is important because it provides a direct reference point for evaluating classification performance on the same multi-source dataset structure.

Compared with conventional CNN models, the proposed MS-GHOST-RAAE framework does not rely only on standard convolutional layers for feature extraction. Classical CNN models can learn useful spatial features, but they may require many convolution operations to obtain strong representations. Transfer learning models such as ResNet and VGG can provide high classification performance, but they are usually deeper and may need higher computational cost, memory usage, and training time. Attention-based CNN models improve feature selection by focusing on important image regions; however, they generally use attention only as an additional module inside a CNN structure. Autoencoder-based models can learn compact representations, but they may not always capture tumor-related discriminative features strongly enough when used alone. GhostNet-like lightweight models reduce redundant convolutional operations and produce efficient feature maps, but they are mostly designed as general lightweight CNN architectures. In contrast, the proposed MS-GHOST-RAAE framework combines multi-stage preprocessing, wavelet-based enhancement, multi-scale GHOST feature extraction, residual learning, attention refinement, autoencoder-based representation learning, and machine learning classification in a single pipeline. Therefore, the proposed method aims to obtain compact, discriminative, and computationally efficient features for multi-class brain tumor MRI classification on a heterogeneous combined dataset.

In contrast, the proposed method employs a more comprehensive preprocessing step prior to the feature extraction phase. This step consists of grayscale transformation, Otsu thresholding, region of interest extraction, color-based segmentation, masking, Canny edge detection, contour identification, and wavelet transformation. These processes are designed to highlight tumor-related regions and reduce unnecessary background information. Following the preprocessing, the proposed MS-GHOST-RAAE architecture extracts distinctive deep features, and these features are classified using machine learning classifiers.

Compared with Celik and Inik (2024) [27], the proposed method increases the classification accuracy from 97.93% to 98.75% on the combined Figshare + Br35H + SARTAJ dataset. This development demonstrates that the components used in the proposed method contribute to the classification success. Special image preprocessing steps make tumor regions more distinct. Wavelet transform helps extract more useful information from the image. Multi-scale GHOST feature extraction retrieves key features more efficiently. The residual learning structure ensures more stable model operation.

The attention mechanism helps the model focus on important tumor-related regions. Therefore, the proposed hybrid method offers a more effective classification approach for heterogeneous MRI data from different sources.

3. Materials and Methods

This section describes the proposed hybrid method. The method was used for multi-class brain tumor MRI classification on the Figshare + Br35H + SARTAJ combined dataset. The general workflow consists of three main stages. The first stage involves image preprocessing. This stage is used to make tumor-related regions more prominent. In the second stage, deep features are extracted using the MS-GHOST-RAAE architecture. In the third stage, the extracted features are classified using conventional machine learning algorithms. Figure 1 shows the entire workflow of the proposed method. The blocks shown in green in the figure represent the key contributions of this study. These are the custom preprocessing process, wavelet-based enhancement, and the MS-GHOST-RAAE feature extraction architecture.

The proposed MS-GHOST-RAAE framework is different from standard CNN-based and transfer learning-based methods because it combines several useful components in one hybrid structure. The preprocessing stage enhances tumor-related regions and reduces unnecessary background information. The wavelet transformation improves spatial and frequency-based image information. The multi-scale GHOST module extracts efficient feature maps with fewer redundant convolutional operations. Residual connections preserve important spatial details and support stable training. The attention mechanism helps the model focus on discriminative tumor features. In the final stage, the extracted deep features are evaluated using machine learning classifiers. Thus, the proposed framework combines preprocessing, lightweight feature extraction, residual learning, attention-based refinement, autoencoder representation, and machine learning classification for robust multi-class brain tumor MRI classification.

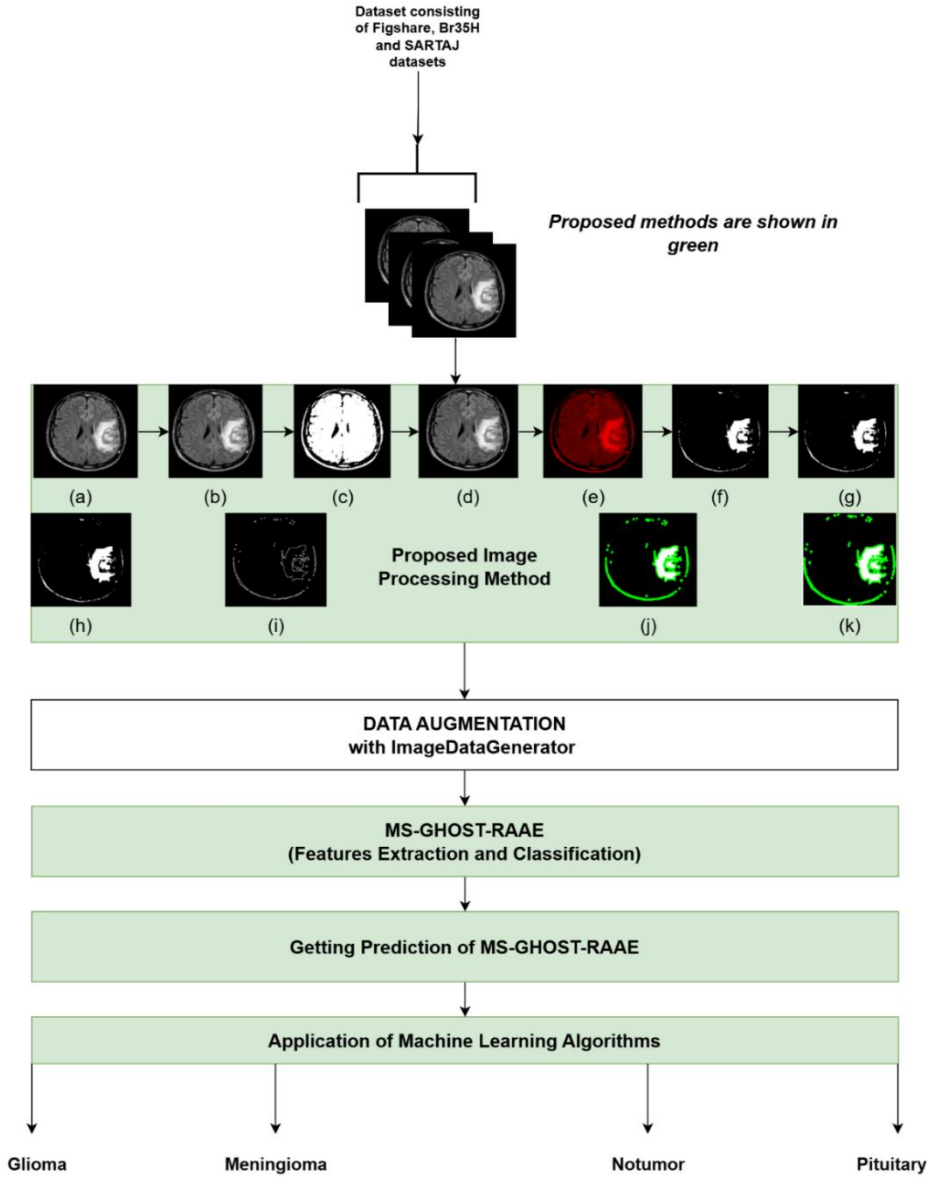

Figure 1. Flowchart of the proposed hybrid brain tumor MRI classification framework on the combined Figshare + Br35H + SARTAJ dataset. The green blocks indicate the main contributions of this study.

Fig. 1 presents the end-to-end processing flow of the proposed approach. First, MRI images from Figshare, Br35H, and SARTAJ data sources are combined into an integrated multi-class dataset consisting of glioma, meningioma, no-tumor, and pituitary tumor categories. Then, a multi-stage preprocessing procedure is applied to increase the visibility of tumor-associated areas and reduce background effects. After the preprocessing steps and wavelet-based transformation are completed, the MS-GHOST-RAAE model obtains essential and distinctive deep feature representations. Finally, these extracted features are fed into conventional machine learning classifiers, thus performing multi-class brain tumor prediction.

3.1. Image Processing for Tumor Region Segmentation

This section describes a multi-stage image preprocessing procedure applied to MRI images from a combined dataset of Figshare + Br35H + SARTAJ sources to enhance the visibility of tumor-associated regions. These preprocessing steps aim to improve the visibility of tumor structures before feature extraction and classification. The techniques used are performed in a specific order to ensure the most accurate identification of the tumor area. The most critical aspect of this process is the effective application of segmentation, considering both large and small protruding structures in the tumor region. Otherwise, the tumor area cannot be sufficiently separated from non-tumor tissues, and the model's learning process cannot be successfully completed.

In the proposed preprocessing pipeline, each image processing step has a specific technical role. Otsu thresholding is used to automatically determine an optimal threshold value from the image histogram and separate possible tumor-related regions from the background. After thresholding, ROI extraction is applied to focus only on the most informative part of the MRI image and remove unnecessary surrounding areas. Canny edge detection is then used to detect sharp intensity changes and highlight the boundaries of tumor structures. After edge detection, contour detection is applied to identify connected boundary regions and describe the shape of the possible tumor area more clearly. Finally, wavelet transformation with VisuShrink is used to reduce noise and preserve important spatial and frequency information. This step helps strengthen edge, texture, and structural details before feature extraction. Therefore, these preprocessing operations make tumor-related regions more visible and provide cleaner input images for the proposed MS-GHOST-RAAE model.

3.1.1. BGR to GRAY

RGB is actually a BGR image whose 4th byte is one byte. So procedurally converting BGR to GRAY is just like converting RGB to GRAY. Thanks to this cycle, the morphological characteristics, which is also our goal, can be better determined. $n \times m \times 3$ morphological features are emphasized by reducing an image to one channel. In our study, we use the averaging method to convert BGR to grayscale. It is shown in Fig. 2 (b). The mathematical formula is given in Eq. (1).

$$Grayscale = (R + G + B)/3 \tag{1}$$

3.1.2. Binary and otsu's thresholding transformation process

In this method, pixels below the determined threshold value in the image are assigned as zero, while pixels above the threshold value are represented as one. This process is used for object detection, segmentation, and noise reduction on images. In the Otsu binary method, the threshold value is automatically determined by considering the value between two peaks in the image histogram. In other words, this method automates the thresholding process by selecting a global threshold value from the histogram. Thus, the tumor region on the image can be represented with low pixel values and defined more clearly. This process is shown in Figure 2(c). The mathematical expressions for this process are given in Eqs. (2–5).

$$\sigma_w^2(t) = q_1(t)\sigma_1^2(t) + q_2(t)\sigma_2^2(t) \tag{2}$$

Where in;

$$q_1(t) = \sum_{i=1}^{t} P(i)\ ,\ q_2(t) = \sum_{i=t+1}^{I} P(i) \tag{3}$$

$$\mu_1(t) = \sum_{i=1}^{t} \frac{iP(i)}{q_1(t)}\ ,\ \mu_2(t) = \sum_{i=t+1}^{I} \frac{iP(i)}{q_2(t)} \tag{4}$$

$$\sigma_1^2(t) = \sum_{i=1}^{t} [i - \mu_1(t)]^2 \frac{iP(i)}{q_1(t)}\ ,\ \sigma_2^2(t) = \sum_{i=t+1}^{I} [i - \mu_2(t)]^2 \frac{iP(i)}{q_2(t)} \tag{5}$$

3.1.3. Bounding rectangular and ROI process

Bounding rectangular process draws a rectangle on the part of the image you want to emphasize. That is, the part to be emphasized is highlighted in the image. It works with four parameters. These are denoted by x, y, w, h.

x: The coordinate value of the x-axis,

y: The coordinate value of the y-axis,

w: width,

h: height.

In the ROI process, automatically a rectangle is drawn around the rectangle to be drawn in the previous process, that is, around the part to be highlighted. In our paper, the parameters in the bounding rectangular process were selected according to the Binary and otsu thresholding transformation process, and the ROI process was applied to the BGR image. It is shown in Fig. 2 (d).

3.1.4. Color segmentation on ROI process

At this stage, the color segmentation process is performed on the ROI image obtained. In this process, the ROI image is first converted to HSV. Afterwards, the upper and lower color thresholds are determined and masking is performed according to these thresholds. These thresholds are [0, 0, 152] for the lower and [179, 255, 255] for the upper. It is shown in Fig. 2 (e).

3.1.5. Image masking

Masking is an image processing technique used to replace a larger image with a defined smaller image portion. Masking is a process underlying many types of image processing, including edge detection, motion detection, and noise reduction. It is shown in Fig. 2 (f).

3.1.6. Blurring and Canny detection process

The GaussianBlur filter applies a smoothing process on the image. This method takes as parameters a source image of type mat object, a result of type mat, the blur value to be applied of type Size (also called kernel size), and the kernel standard deviation called SigmaX. This makes it easier to apply canny detection to the softened image. Then canny detection process is used to detect the edges of the tumor region. With edge detection on an image, objects in that image can be detected, counted, and characterized. In basic terms, edge detection algorithms are determined by differentiating the color values of the pixels on the image. It is shown in Fig. 2 (g) and (h). This can clearly show us the edges of the tumor area. The mathematical formula is as follows in Eq. (6)

$$G(X) = \frac{1}{\sqrt{2\pi\sigma^2}} e^{\frac{x^2+y^2}{2\sigma^2}} \tag{6}$$

Wherein, x and y are the coordinates of the image and σ is the standard deviation of the distribution.

3.1.7. Contour detection process

The final step of the segmentation process is to draw a line connecting all points with the same intensity along the boundary of the image to the edges of the tumor region whose edges have been determined, and it provides the computer with great convenience in learning the tumor region. It is shown in Fig. 2 (i) and (j).

3.1.8. Wavelet transform with VisuShrink process

This process effectively suppresses noise by analyzing the image in both spatial and frequency domains. In the spatial domain, pixel values are represented as matrices, and the transformation detects variations within these matrices. In the frequency domain, the method evaluates how rapidly pixel intensities change: high-frequency components correspond to abrupt intensity variations such as edges, whereas low-frequency components represent smoother, homogeneous regions.

The wavelet transform jointly captures spatial and frequency information by providing low-resolution representations at low frequencies and high temporal resolution at high frequencies. During this process, the images are first passed through high-pass and low-pass filters to generate approximation and detail coefficients. The approximation coefficients are computed using the relation defined in Eq. (7), while the horizontal, vertical, and diagonal detail components are produced through the filter operations described in Eqs. (8), (9), and (10), respectively. Each decomposition level yields four sub-bands, where approximations describe the global structure of the image and detail components encode directional variations. Through this multilevel decomposition, both filtering and compression are achieved, as illustrated in Fig. 2(k).

$$S_{j,v} = 2^{1/2} \sum_{k} hh(l-2v) S_{j+1,l} \tag{7}$$

$$W^1{}_{j,v} = 2^{1/2} \sum_{k} hg(l-2v) S_{j+1,l} \tag{8}$$

$$W^2{}_{j,v} = 2^{1/2} \sum_{k} gh(l-2v) S_{j+1,l} \tag{9}$$

$$W^3{}_{j,v} = 2^{1/2} \sum_k gg(l-2v) S_{j+1,l} \tag{10}$$

Wherein, $k=1,2,3$ is the $S_{j,k}$ scaling and $W^k{}_{j,k}$ wavelet coefficients for the signal $f(t)$ given at scale j. The low-pass filter is denoted by h and the high-pass filter by g.

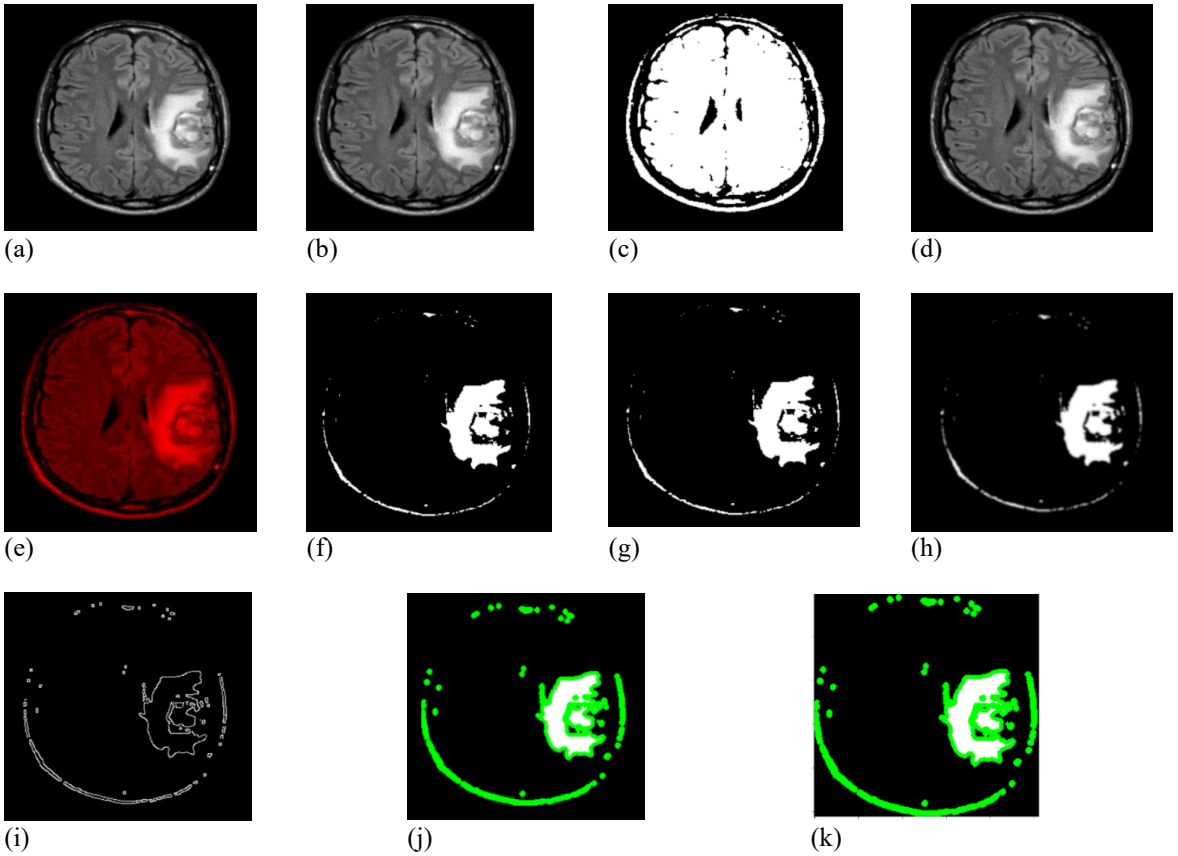

Figure 2. Preprocessing stages applied to brain tumor MRI images from the combined Figshare + Br35H + SARTAJ dataset: (a) original image, (b) grayscale image, (c) binary and Otsu thresholding, (d) ROI image, (e) HSV image, (f) color segmentation with HSV image, (g) masked image, (h) blurred image, (i) Canny edge detection image, (j) contour image, and (k) wavelet transformation with VisuShrink.

Fig. 2 shows the preprocessing steps applied before feature extraction. First, a grayscale transformation is performed. Then, binary thresholding and Otsu thresholding are applied. These steps make tumor-related regions more prominent. ROI extraction, color segmentation, and masking operations reduce unnecessary background information. Blurring, Canny edge detection, and contour detection make structural boundaries clearer. Finally, wavelet transformation is applied with VisuShrink. This process strengthens the spatial and frequency information of the image. Thus, the proposed MS-GHOST-RAAE model can extract more distinctive features.

3.2. Feature Extraction with MS-GHOST-RAAE

Accurate classification of brain tumor MRI images is crucial for assessing patient health. However, performing this process manually, even with only specialists, can be time-consuming and costly. The proposed MS-GHOST-RAAE method offers a more efficient option. This method performs feature extraction automatically. Feature extraction is a complex process, making it difficult to perform manually on large datasets. Convolutional neural networks (CNNs) are commonly used for feature extraction because they can directly learn important information from images and can progressively extract simple and complex features. As stated in [28-35], CNN architectures extract distinguishing features by passing images through multiple convolution layers, and these features are then used in classification or prediction processes. Their ability to automatically identify relevant features and provide high prediction accuracy are among the main reasons for the widespread preference of CNN-based methods. In this study, the proposed MS-GHOST-RAAE-based feature extraction framework is evaluated on a combined dataset created from Figshare + Br35H + SARTAJ sources and compared with transfer learning-based models such as ResNet50, ResNet101, ResNet152, and VGG16. The main objective of this comparison is to determine whether the proposed lightweight hybrid representation approach can provide competitive or superior classification performance on a heterogeneous and multi-source MRI dataset.

3.3 Multi-Scale GHOST-RAAE Architecture

The multi-scale GHOST-residual attention autoencoder architecture will be explained in this section with figures and mathematical equations. First, the autoencoder structure used below and how many blocks it consists of are shown in Fig. 3. The purpose of this block is to encode the images in a lower dimensional form to reduce noise, reduce size, and eliminate features with insignificant variance and emphasize important features.

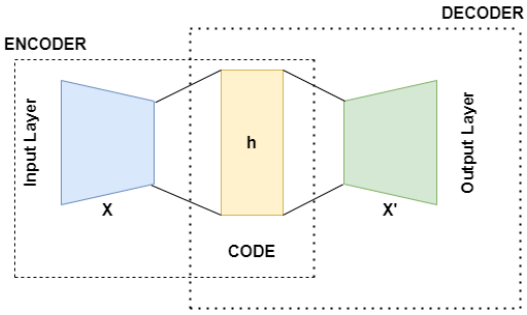

Figure 3. Simple autoencoder architecture

In *X:* input data, *h=f(X),* the encoder function converts the input data into a code (h) representation, $h_{residual} = h + X$, the residual links sum the original input data with the code. This allows the network to be deeper, $h_{attended} = Attention(h_{residual})$, Attention mechanism learns to focus on specific regions in the feature map using residual connections, $\hat{X} = g(h_{attended})$, the Decoder function decodes the focused code in a similar way to the original input.

This Fig. 3, illustrates the structure of the proposed residual–attention autoencoder, where the encoder compresses the input into a latent representation and residual connections preserve essential information by directly adding the input to the encoded features. The attention mechanism refines these features by emphasizing informative regions of the latent space, after which the decoder reconstructs an output that mirrors the original input. This design enhances representation quality while maintaining stability in deeper architectures.

Fig. 4 presents the residual attention autoencoder architecture in more detail.

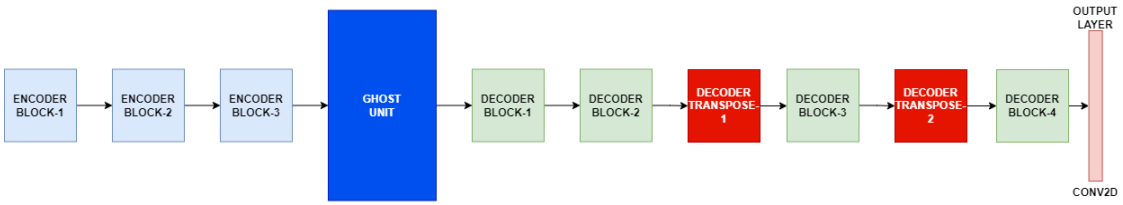

Figure 4. Detailed version of the proposed residual attention autoencoder architecture

Fig. 4 presents the general structure of the proposed residual attention autoencoder architecture. Encoder blocks progressively compress the input feature maps; then the GHOST unit produces efficient multi-scale representations with lower computational cost. Subsequently, the decoder structure reconstructs the feature space through successive decoding and transposition convolution layers, enabling the recovery of spatial resolution. In this process, residual features driven by the attention mechanism are also included in the model. The final convolution layer produces the improved output representation to be used in the next classification stage.

The input data is (120,120,3). In the encoder block, after conv2d, batch normalization, activation, attention global average pooling, attention sigmoid, and expansion dimension twice, the output dimension becomes (1,1,64). Then the residual enters the conv2d layer and its size becomes (120,120,64). Then the output from the 2nd dimension expansion layer is multiplied by the output from the activation layer. The result of the multiplication is then summed with the residual conv2d layer and the encoder block-1 ends. The mathematical expression of this process is as follows in Eqs. (11-20)

$$X \epsilon R^{120,120,3} \tag{11}$$

$$H_1 = CONV2D(X) \tag{12}$$

$$H_2 = f_b(H_1) \tag{13}$$

$$H_3 = f_r(H_2) \tag{14}$$

$$H_4 = f_{AGAP}(H_3), \tag{15}$$

$$H_5 = f_{AS}(H_4), \tag{16}$$

$$H_6 = f_{EX}(f_{EX}(H_5)), \quad (17)$$

$$R_1 = residualCONV2D(H_6), \quad (18)$$

$$R_2 = R_1 + X, \quad (19)$$

$$Q = (R_2\ X\ H_6) + R_2, \quad (20)$$

Wherein; X is the input data of the encoder block layer, $f_b(*)$ is the batch normalization, $f_r(*)$ is the ReLu activation function, $f_{AGAP}(*)$ is the attention global average pooling, $f_{AS}(*)$ is the attention sigmoid and $f_{EX}(*)$ is the dimension expansion.

Fig. 5 shows the detailed shape of the encoder block.

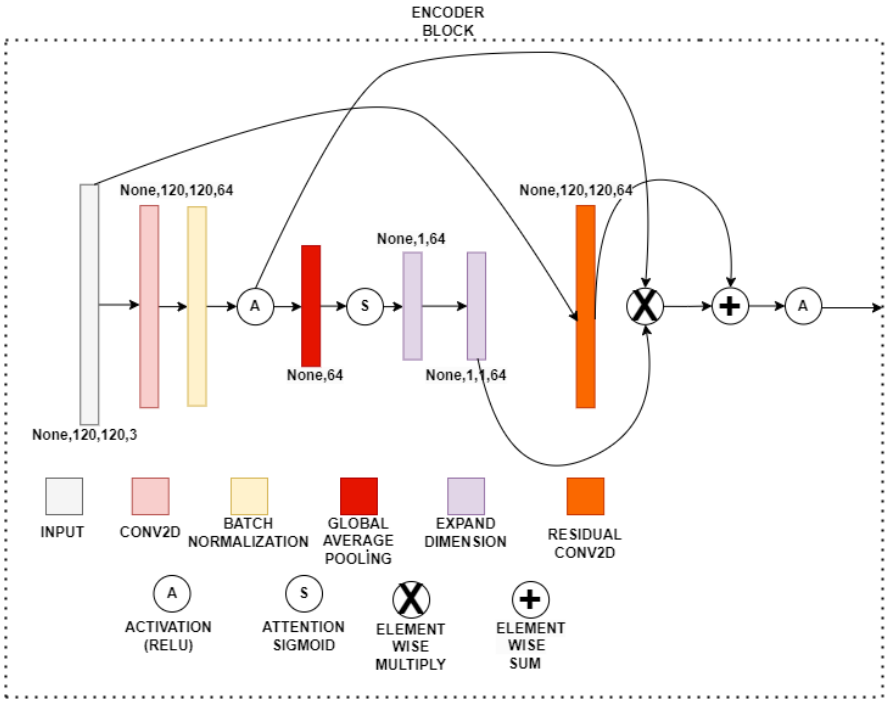

Figure 5. Detailed shape of encoder block

Fig. 5 shows the internal structure of the encoder block used in the proposed architecture. In this block, low-level features are progressively extracted through convolution, aggregate normalization, and activation layers. These features are then reorganized using global average pooling and a channel-based attention mechanism; the generated significance weights are expanded and multiplied by feature maps, thus highlighting prominent regions more strongly. In addition, the residual convolution path contributes to the preservation of spatial information and a more stable gradient flow. In the final stage, both the information from the residual link and the outputs enhanced by the attention mechanism are combined through element-based summation. This structure ensures the acquisition of more robust and distinctive feature representations within the proposed architecture.

In the decoder block, the input data from the GHOST module is (8,8,128). In the decoder block, after conv2d, batch normalization, activation, attention global average pooling, attention sigmoid, and expansion dimension twice, the output dimension becomes (1,1,128). Then the residual enters the conv2d layer and its size becomes (8,8,128). Then the output from the 2nd dimension expansion layer is multiplied by the output from the activation layer. The result of the multiplication is then summed with the residual conv2d layer and the encoder block-1 ends. The mathematical expression of this process is as follows in Eqs.(21-30).

$$X_g \epsilon R^{8,8,128} \quad (21)$$

$$H_{1d} = CONV2D(X), \quad (22)$$

$$H_{2d} = f_b(H_{1d}), \quad (23)$$

$$H_{3d} = f_r(H_{2d}), \quad (24)$$

$$H_{4d} = f_{AGAP}(H_{3d}), \quad (25)$$

$$H_{5d} = f_{AS}(H_{4d}), \quad (26)$$

$$H_{6d} = f_{EX}(f_{EX}(H_{5d})), \quad (27)$$

$$R_{1d} = residualCONV2D(H_{6d}), \quad (28)$$

$$R_{2d} = R_{1d} + X_g, \quad (29)$$

$$Q_d = (R_{2d}\ X\ H_{6d}) + R_{2d}, \quad (30)$$

Wherein; X_d is the input data of the decoder block layer, $f_b(*)$ is the batch normalization, $f_r(*)$ is the ReLu activation function, $f_{AGAP}(*)$ is the attention global average pooling, $f_{AS}(*)$ is the attention sigmoid and $f_{EX}(*)$ is the dimension expansion.

Fig. 6 shows the detailed shape of the decoder block.

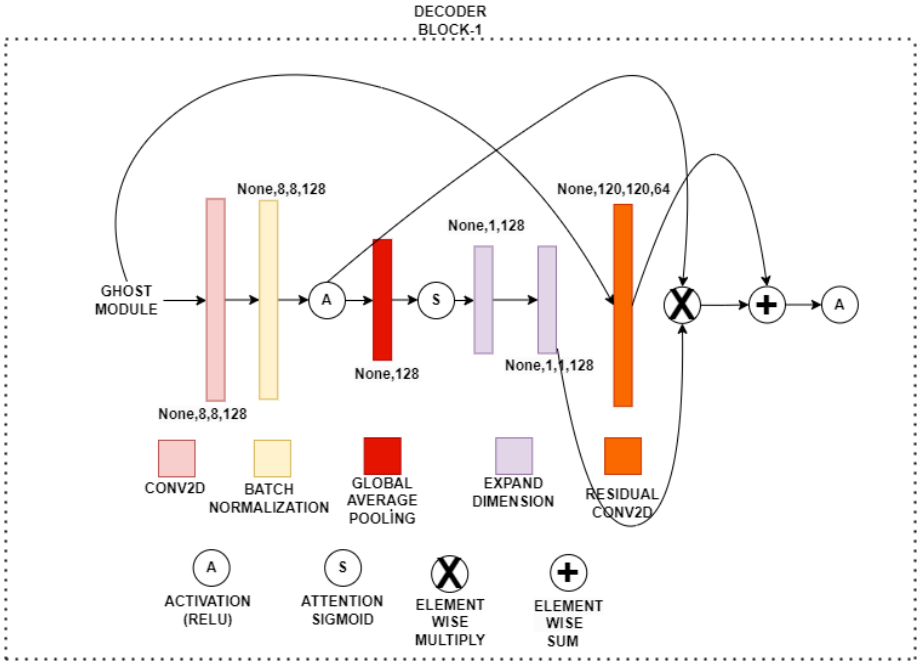

Figure 6. Detailed shape of encoder block

Fig. 6 shows the structure of the decoder block. This block generally reflects the encoder structure but also includes the GHOST module to produce efficient feature representations in the upsampling process. The expanded feature maps are progressively improved through convolution, aggregate normalization, and activation layers. The channel attention mechanism is implemented through global average pooling and dimensionality expansion operations, highlighting more important channels. In addition, the residual linkage path contributes to the preservation of fundamental spatial information. Element-based multiplication and summation operations performed in the final stage combine features enhanced by the attention mechanism with residual features, thus enabling more accurate reconstruction of high-resolution representations during the decoding phase.

In decoder transpose, the input data from decoder block-2 is (4,4,64). The output dimension becomes (1,1,128) after conv2d transpose, conv2d, batch normalization, activation, attention global average pooling, attention sigmoid, and expand dimension twice in decoder transpose. Then the residual enters the conv2d layer and its size becomes (8,8,128). Then the output from the 2nd dimension expansion layer is multiplied by the output from the activation layer. The result of the multiplication is then summed with the residual conv2d layer and the decoder transpose ends. The mathematical expression of this process is as follows in Eqs.(31-40).

$$X_t \epsilon R^{8,8,128} \quad (31)$$

$$H_{1t} = CONV2D(X), \quad (32)$$

$$H_{2t} = f_b(H_{1t}), \quad (33)$$

$$H_{3t} = f_r(H_{2t}), \quad (34)$$

$$H_{4t} = f_{AGAP}(H_{3t}), \quad (35)$$

$$H_{5t} = f_{AS}(H_{4t}), \quad (36)$$

$$H_{6t} = f_{EX}(f_{EX}(H_{5t})), \quad (37)$$

$$R_{1t} = residualCONV2D(H_{6t}), \quad (38)$$

$$R_{2t} = R_{1t} + X_t, \quad (39)$$

$$Q_t = (R_{2t}\ X\ H_{6t}) + R_{2t}, \tag{40}$$

Wherein; X_t is the input data of the decoder transpose layer, $f_b(*)$ is the batch normalization, $f_r(*)$ is the ReLu activation function, $f_{AGAP}(*)$ is the attention global average pooling, $f_{AS}(*)$ is the attention sigmoid and $f_{EX}(*)$ is the dimension expansion.

Fig. 7 shows the detailed shape of the decoder transpose.

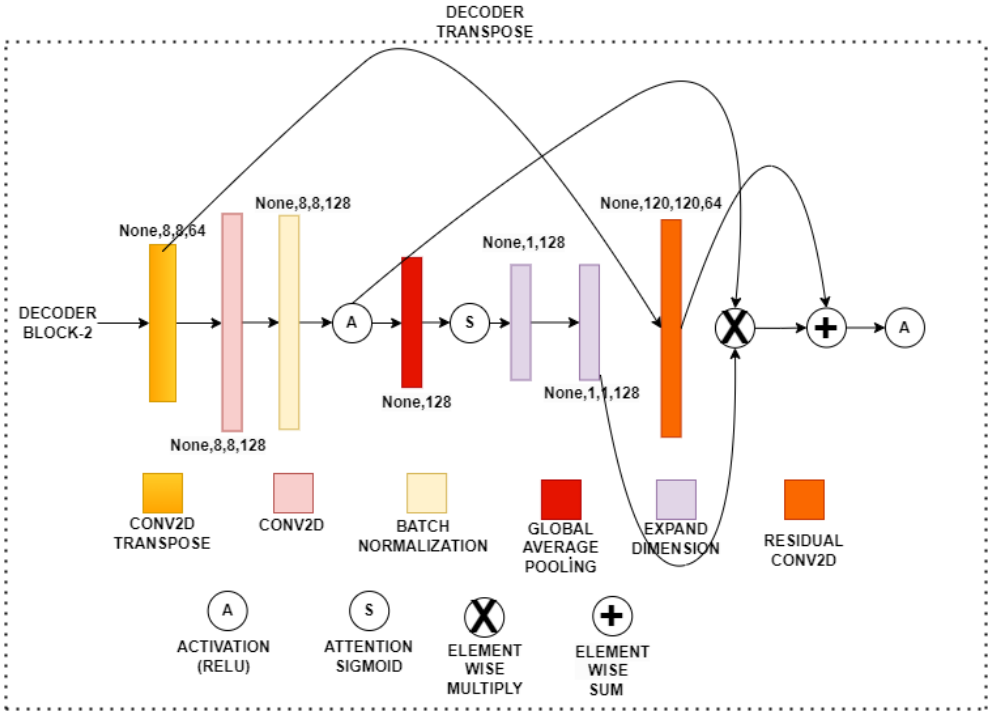

Figure 7. Detailed shape of decoder transpose

Fig. 7 shows that the decoder-transpose block regains spatial resolution through transpose convolution operations. Subsequent layers of convolution, aggregate normalization, and activation progressively improve the upsampled feature maps. The channel attention mechanism is incorporated into the structure via global average pooling and dimensionality expansion operations, allowing the network to focus more on informative channels and suppress less related features. Furthermore, the convolution path helps preserve fundamental structural information and supports a more stable gradient flow throughout the training process. Finally, features enhanced by the attention mechanism are combined with information from the linkage via element-based multiplication and summation operations, resulting in a more coherent and distinctive representation that supports effective reconstruction in the remaining decoding stages.

3.4. Attention Mechanism and Residual Blocks in The Proposed MS-GHOST-RAAE Model

The proposed MS-GHOST-RAAE model utilizes an attention mechanism and residual blocks. These structures help the model extract better features because MRI images from Figshare, Br35H, and SARTAJ data may differ. The attention mechanism highlights important tumor-related regions, while residual blocks help preserve fundamental spatial information in the image. Thus, the model can learn more stable, meaningful, and informative features. Furthermore, the GHOST-based attention mechanism generates efficient feature maps with lower computational cost. Instead of relying solely on high-cost transformations, this structure first generates basic feature maps using standard convolution, and then produces additional ghost feature maps through light convolutions.

Primary Convolution: The first step is to generate the primary feature maps X_p from the input X. W_p represents the weight.

$$X_p = CONV2D(X; W_p), \tag{41}$$

1. GHOST Convolutions: Additional GHOST feature maps are then generated using X_p

$$X_g^i = CONV2D(X; W_g^i), \tag{42}$$

Here W_g^i represents each set of GHOST convolutional filters and i are the different ratios used to generate GHOST channels.

2. Use of Ratios: Each GHOST convolutional layer (X_g^i) uses different rates (r_i) to capture different aspects of the input. These ratios divide the output of the primary convolutional layer (X_p) into smaller partitions, providing different information densities:

$$X_g^i = CONV2D\left(X_p; \frac{W_p}{r_i}\right), \tag{43}$$

Here; $\frac{W_p}{r_i}$, Represents a set of convolutional filters reduced by r_i. This allows each GHOST convolutional layer to capture a different information density and spread.

3. Channel Concating: Finally, the primary and GHOST feature maps are combined.

$$X_{out} = Concat\left(\left[X_p, X_g^1, X_g^2, \ldots., X_g^n\right]\right), \tag{44}$$

Here; X_p represents primary feature map and X_g^n represents GHOST feature maps

This process, formalized in Eqs. (41–44), allows the model to capture diverse information densities through multiple convolutional ratios and subsequently concatenate all feature maps to obtain a richer representation.

Conventional attention mechanisms, by contrast, depend on global average pooling and multilayer perceptrons, as expressed in Eqs. (45–48), which increases parameter count and computational overhead. The GHOST attention, therefore, provides a more efficient alternative by amplifying informative local patterns without the need for expensive transformations.

1. Global Attention: It extracts global mean values of input feature maps using GAP (Global Average Pooling). GAP stands for global average pooling and is often used in convolutional neural networks (CNN). GAP averages all values in each channel of the input feature maps, thus producing a single value for each channel.

$$Z_C = \frac{1}{H * W} \sum_{i=1}^{H} \sum_{j=1}^{W} x_{i,j,c} \tag{45}$$

Here;

$x_{i,j,c}$, pixel value at position *(i,j)* in the ith channel,

H and *W* are the height and width of the input feature maps,

Zc, Average value of c-th channel.

2. Compresses and excites these average values using MLP. It stands for multilayer perceptron. This is a simple neural network structure consisting of one or more fully connected layers. It usually works like this:

$$h_1 = \delta(W_1 x + b_1), \tag{46}$$

$$h_2 = \delta(W_2 h_1 + b_2), \tag{47}$$

$$y = \sigma(W_3 h_2 + b_3), \tag{48}$$

Here;

W_i and b_i are the weights and biases of the i-th layer,

δ is the activation function (e.g., ReLU).

σ is the activation function usually used for the final output (e.g. sigmoid or softmax). (The simplest MLP is represented.)

This shows that the ordinary attention mechanism with mathematical equations is computationally more expensive than our proposed attention mechanism.

Nowadays, blocks enhance the model's learning capacity, particularly in deeper architectures, by improving gradient flow and making the training process more stable. Remaining connections reduce the vanishing gradient problem by allowing input information to be directly passed to subsequent layers, while batch normalization contributes to more balanced updates and accelerates convergence. Used in conjunction with GHOST modules and attention processes, these residual structures enable the model to generate richer, more stable, and more distinctive feature representations.

In general, the combined use of GHOST convolutions, the light attention mechanism, and residual connections increases feature diversity and contributes to a more stable training process. Within the context of a combined dataset created from

Figshare + Br35H + SARTAJ sources, this design enables the proposed model to extract distinctive features from heterogeneous MRI images while keeping computational costs at a practical level.

3.5. Classification with The Proposed MS-GHOST-RAAE Model

After feature extraction by MS-GHOST-RAAE, the obtained deep feature vectors are used for multiclass classification on the combined Figshare + Br35H + SARTAJ dataset. The classification task includes four classes: glioma, meningioma, no-tumor, and pituitary tumor. Since the problem is formulated as a multiclass classification task, sparse categorical cross-entropy is used as the loss function in the deep learning stage. Its mathematical formulation is given in Eq. (49).

$$SCCE = -\sum_{i}^{n} (\delta_{i,y}.\log(\hat{y}_i)) \tag{49}$$

Where in; i represents the class indices. $\delta_{i,y}$ is the kronecker delta and takes the value 1 if i and y are equal, 0 otherwise. $\hat{y}_i$ is the probability for the predicted class i.

In the proposed framework, MRI images are first converted into matrix representations and then passed through convolutional layers to obtain feature maps. These resulting feature maps are reduced to more compact feature vectors through a global average pooling operation. Batch normalization is applied to ensure a more stable learning process, and fully connected layers transform the extracted feature representations into class-specific outputs. In the final stage, the classification layer generates four probability values corresponding to the glioma, meningioma, no-tumor, and pituitary tumor classes. The detailed structure of the classification layer is shown in Fig. 8.

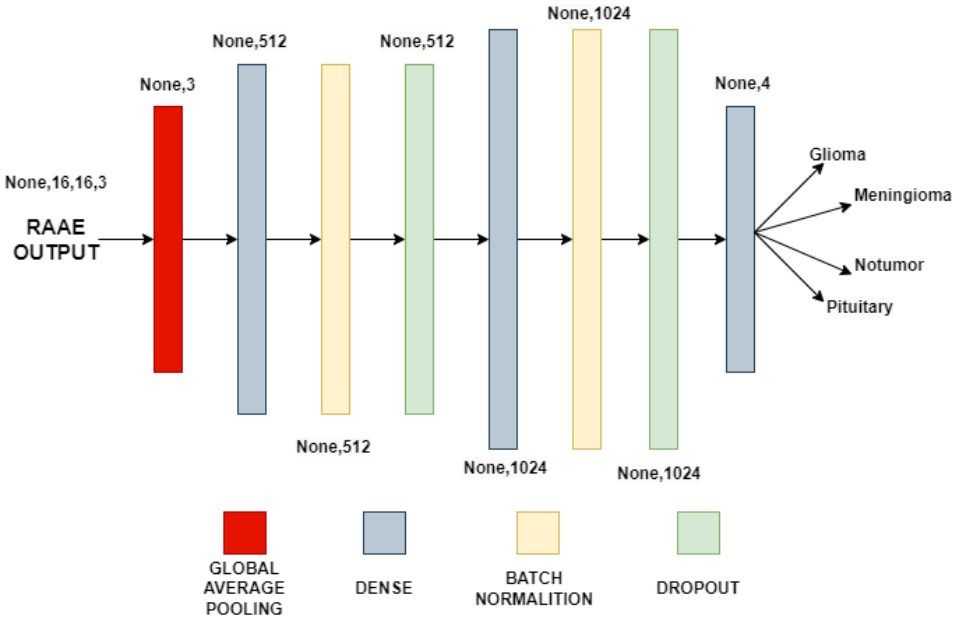

Figure 8. Detailed shape of classification layers

Fig. 8 shows the classification phase following the feature extraction process performed with MS-GHOST-RAAE. In this phase, global average pooling transforms spatial feature maps into shorter and more compact feature vectors. These resulting vectors are passed through successive fully linked layers that are stabilized by batch normalization and optimized with dropout to reduce overfitting. The final fully linked layer generates four output probabilities representing glioma, meningioma, no-tumor, and pituitary tumor classes. This structure enables multi-class prediction on the Figshare + Br35H + SARTAJ combined dataset based on the distinctive features extracted by the proposed architecture.

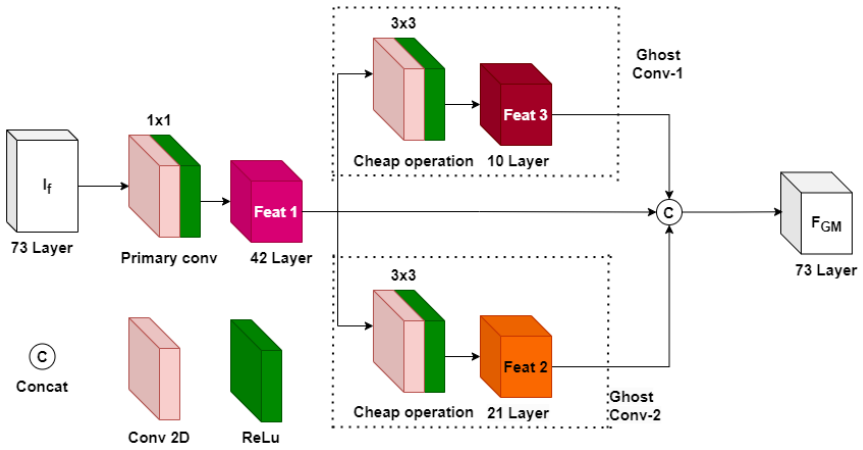

Figure 9. Detailed Multi-scale GHOST unit

Fig. 9, shows that the structure of the multi-scale GHOST module includes 1x1 and 3x3 convolution operations. In the module mentioned, unnecessary features are done by channel removal. It then learns the redundant channels that are eliminated from the feature map obtained by the convolution process. The most recently extracted feature map is linked to the original feature map. This module not only eliminates similar features but also draws more attention to weighted feature channels. Furthermore, it reduces the number of parameters and the computational cost of the network. It can be expressed as follows in Eqs. (50-53).

$$F_{GM}=concat(Feat1,Feat2,Feat3) \quad (50)$$

$$Feat1=W1x1(If) \quad (51)$$

$$Feat2=W3x3(Feat1) \quad (52)$$

$$Feat3=W3x3(Feat1) \quad (53)$$

Wherein, I_f represents the input feature map of the GHOST module, *Feat1* represents the primary convolution with 1x1 convolution and relu activation function operation, and *Feat2* and *Feat3* represent the cheap process with 3x3 convolution and relu activation function operation. F_{GM} is the output of the GHOST module.

Fig. 10 shows the input, encoder output, and decoder output images of our proposed model.

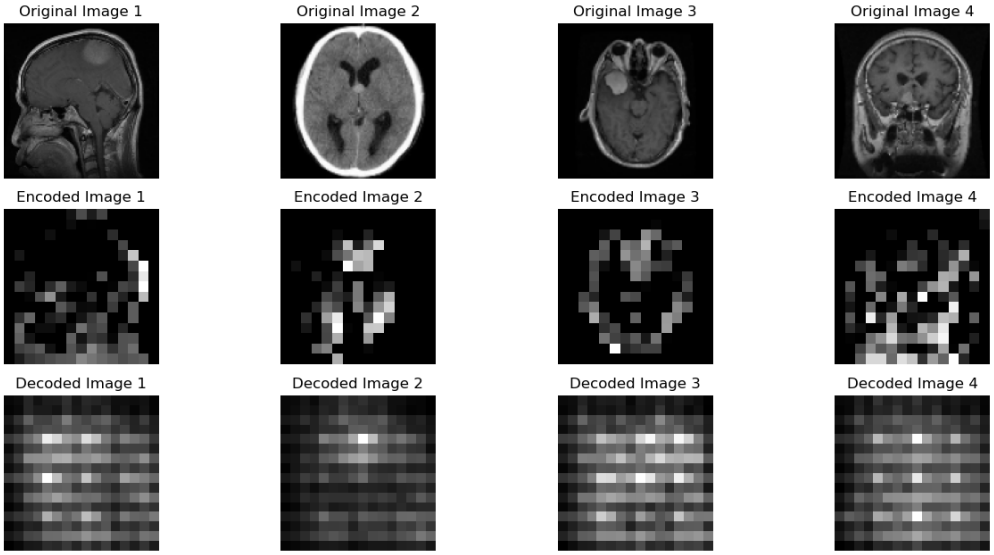

Figure 10. Original image, output images of the encoder structure, and output images of the decoder structure

3.6. Machine Learning Classifiers for Feature-Based Classification

The deep features extracted from the combined Figshare + Br35H + SARTAJ MRI images by MS-GHOST-RAAE are flattened and used as input to conventional machine learning classifiers. The evaluated classifiers include Multi-Layer Perceptron (MLP) [36], Gradient Boosting Classifier (GBC) [37], AdaBoost Classifier (ABC) [38], Support Vector Machine (SVM) [39], Logistic Regression (LR) [40], Naive Bayes (NB) [41], Decision Tree (DT) [42], Random Forest (RF) [43], K-Nearest Neighbors (KNN) [44], and a stacking-based classifier (CLF). In the stacking classifier, Logistic

Regression is used as the meta-model to generate the final prediction by combining the outputs of the base learners. The base learners consist of Naive Bayes, Multi-Layer Perceptron, and Support Vector Machine. Cross-validation is then applied to evaluate the classification performance of these machine learning algorithms in an objective and reliable manner.

3.7. Cross-Validation for Machine Learning Classifiers

To ensure reliable performance evaluation on a combined dataset derived from Figshare, Br35H, and SARTAJ sources, k-fold cross-validation was applied to machine learning classifiers. This approach prevents model performance from being solely dependent on a single training-test split, allowing for a more objective evaluation of the extracted feature representations. In the k-fold cross-validation process, the dataset is randomly shuffled and divided into k equal subsets. In each iteration, one of these subsets is used for validation or testing, while the remaining subsets are used for training. This process is repeated k times, with each subset serving as a validation/test set once. The final performance value is calculated by averaging the results obtained across all folds.

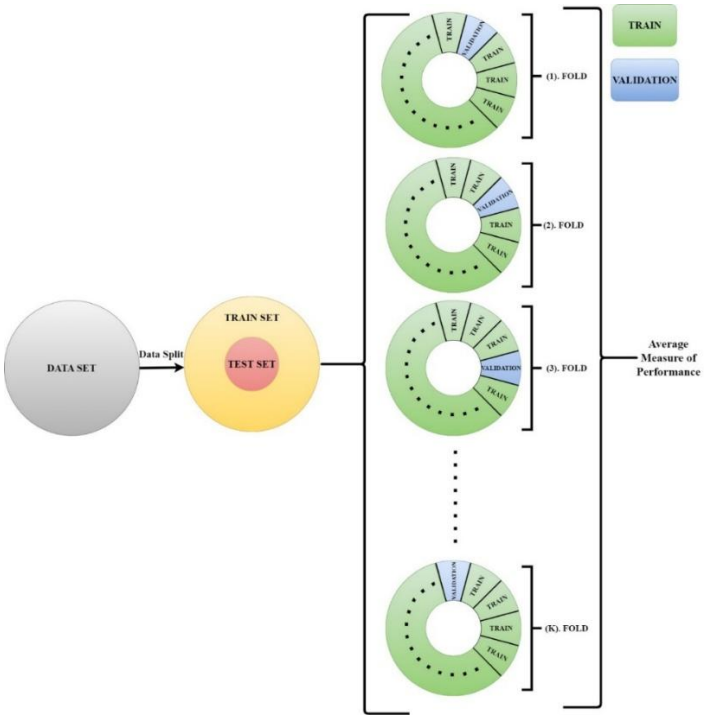

Figure 11. Image of cross-validation 10-fold technique applied

Fig. 11 illustrates the k-fold cross-validation process. This process was used to evaluate machine learning classifiers on the Figshare + Br35H + SARTAJ combined dataset. First, features extracted using MS-GHOST-RAAE are divided into k subgroups. Each subgroup is then used as either test or validation data. The remaining subgroups are used as training data. This process continues until all subgroups have been used for testing/validation. The final performance value is calculated by averaging the results obtained from all k trials. This allows for a more reliable evaluation of the generalization success of the proposed hybrid method.

4. Experimental Results and Analysis

This section presents the experimental results of the proposed MS-GHOST-RAAE-based hybrid method. Experiments were conducted on a combined dataset created from Figshare + Br35H + SARTAJ sources. Dataset settings are explained during the evaluation process. Ablation experiments were also performed. The success of machine learning classifiers was examined. Comparisons were made with transfer learning-based models. Confusion matrix analyses are presented. Finally, comparisons were made with related studies using the same combined dataset.

4.1. Dataset and Experimental Settings

This study uses a combined brain tumor MRI dataset constructed from Figshare, Br35H, and SARTAJ sources [45]. The dataset is publicly available with a CC0 license and contains 7023 MRI images belonging to four classes: glioma, meningioma, no-tumor, and pituitary tumor. The use of a combined dataset provides a more heterogeneous and challenging evaluation setting than single-source datasets, since images may vary in contrast, acquisition conditions, visual quality, and tumor appearance across different sources.

The dataset was divided into two parts: training and testing. This division was done as 80% training and 20% testing. To prevent data leakage, data augmentation operations were applied only to the training data. Horizontal flipping, vertical flipping, and rotation operations were used to augment the training images. After these operations, the number of training samples reached 8402. Model performance was evaluated using different metrics. These metrics are accuracy, F1-score, precision, sensitivity, processing time, and confusion matrix.

All experiments were conducted in an Anaconda-based PyCharm environment using TensorFlow, NumPy, Scikit-learn, and Pandas. The hardware configuration included an NVIDIA GTX-1060 GPU with 6 GB memory, 16 GB RAM, and an Intel Core i7-7700HQ processor. In the deep learning stage, ReLU activation functions were used in hidden layers, softmax activation was used in the output layer, Adam optimizer was employed for training, the batch size was set to 64, and early stopping was applied with a patience value of 5.

4.2. Comparative Baselines

For comparative evaluation on the combined Figshare + Br35H + SARTAJ dataset, two widely used transfer learning families and their derivatives were selected as baseline models.

ResNet (Residual Networks) and VGG (Visual Geometry Group) derivatives are two important architectures frequently used in transfer learning and general deep learning models.

ResNet:

1) ResNet makes it possible to train deeper networks using "residual connections" or "skip connections". It is stated in the literature that these connections reduce the gradient fading problem that occurs in very deep layers of the network.
2) ResNet variants provide high performance and accuracy for multilayer deep networks. This gives very effective results on large datasets.
3) ResNet, in its various versions (ResNet-18, ResNet-34, ResNet-50, etc.), offers networks of different depths, thus providing suitable options for different tasks and datasets.
4) ResNet has the ability to generalize to a variety of computer vision tasks and performs well on different datasets.

In summary, the reason for choosing ResNet variants is both their performance in successfully reducing gradient losses and their success thanks to their depth. Since we were assertive about reducing gradient losses in the algorithm we proposed, we thought that the most suitable algorithms in this field were ResNet derivatives.

VGG:

1) VGG networks offer a simple and streamlined structure using stacked 3x3 convolution layers. This simplicity makes the model easier to understand and apply.
2) VGG is frequently used for transfer learning. These networks offer a variety of pre-trained models and provide successful results in transfer learning applications.
3) Thanks to their modular structure, VGG models can be easily integrated with other architectures and complex network structures can be created.

In summary, the VGG network is chosen to compare our proposed algorithm on the basis of simplicity and time.

The reason why other methods are not included is that there are too many models and the page limit of the article is taken into account. As mentioned above, basic and effective models in terms of performance are included in the comparison.

These transfer learning models were used as comparative baselines to evaluate whether the proposed MS-GHOST-RAAE-based hybrid framework can provide competitive or superior performance on the combined multi-source MRI dataset. Since the present study focuses only on the combined Figshare + Br35H + SARTAJ dataset, all baseline comparisons in the following sections are reported for this dataset.

4.3. Results of Ablation Experiments

Ablation experiments were conducted to examine the contribution of the core architectural components of the proposed MS-GHOST-RAAE model. In these experiments, performance changes resulting from the removal of specific components from the model were analyzed. The aim was to determine the individual effects of the GHOST mechanism, the attention mechanism, and residual blocks on feature representation and classification performance.

Since the current study focuses solely on a combined dataset created from Figshare + Br35H + SARTAJ sources, all ablation experiments were redesigned based on this dataset. This approach ensures a consistent evaluation process and allows for the comparison of the contribution of each architectural component under the same heterogeneous, multi-source MRI classification scenario.

4.3.1 Ablation experiments on the combined Figshare + Br35H + SARTAJ dataset

Tables 2–4 present the ablation experiment results obtained on the combined Figshare + Br35H + SARTAJ dataset. The findings demonstrate that each component in the proposed architecture contributes to the overall classification performance at different levels. Removing the GHOST mechanism reduces the model's ability to produce efficient multi-scale feature representations, potentially decreasing the discriminative power of the removed features. Disabling the

attention mechanism weakens the model's ability to highlight tumor-related key regions and suppress less informative features. Similarly, removing residual blocks can negatively impact gradient flow and feature information preservation, particularly in the deeper layers of the architecture.

Overall, ablation analysis reveals that the combined use of GHOST modules, attention mechanisms, and residual connections offers a more effective feature extraction strategy for heterogeneous MRI images. Therefore, the full MS-GHOST-RAAE architecture was chosen as the final feature extraction model on the combined dataset.

The ablation results show the individual contribution of each main component in the proposed MS-GHOST-RAAE framework. When the GHOST module is removed, the model loses its ability to generate efficient multi-scale feature maps with reduced redundant convolution operations. This may decrease the quality of the extracted features and increase the computational burden. When the attention mechanism is removed, the model becomes less effective in focusing on tumor-related regions and informative feature channels. Therefore, some important discriminative details may be weakened, which can reduce classification performance. When residual connections are removed, the model has more difficulty preserving spatial information and maintaining stable gradient flow during training. This may lead to less stable learning and weaker feature representation. The wavelet-based preprocessing stage also has an important role because it enhances spatial and frequency information before feature extraction. It helps reduce noise, highlight edges, and make tumor-related structures more visible. Therefore, the combined use of wavelet preprocessing, GHOST modules, residual connections, and attention mechanism provides more compact, stable, and discriminative features for multi-class brain tumor MRI classification.

Table 2. Ablation results for the GHOST mechanism on the combined Figshare + Br35H + SARTAJ dataset

Metric Model	Pre-processing (Proposed method)	Accuracy/std	F1 Score/std	Precision/std	Sensitivity/std	Time(sec)	Total Number of Parameters
MS-RAAE	YES	0.96698	0.96699	0.96699	0.96698	4010	1669479
MS-RAAE+RF	YES	0.95826 / (+/- 0.01323)	0.95837 / (+/- 0.01320)	0.95861 / (+/- 0.01315)	0.95826 / (+/- 0.01323)	4010+3.9466	-
MS-RAAE+SVM	YES	0.96636 / (+/- 0.01087)	0.96636 / (+/- 0.01087)	0.96636 / (+/- 0.01087)	0.96636 / (+/- 0.01087)	4010+0.5572	-
MS-RAAE+NB	YES	0.96324 / (+/- 0.01124)	0.96324 / (+/- 0.01124)	0.96324 / (+/- 0.01124)	0.96324 / (+/- 0.01124)	4010+0.4269	-
MS-RAAE+DT	YES	0.95327 / (+/- 0.01371)	0.95333 / (+/- 0.01368)	0.95341 / (+/- 0.01367)	0.95327 / (+/- 0.01371)	4010+9.0810	-
MS-RAAE+KNN	YES	0.95140 / (+/- 0.01285)	0.95156 / (+/- 0.01272)	0.95208 / (+/- 0.01200)	0.95140 / (+/- 0.01285)	4010+0.8192	-
MS-RAAE+LR	YES	0.96636 / (+/- 0.01105)	0.96635 / (+/- 0.01105)	0.96642 / (+/- 0.01100)	0.96636 / (+/- 0.01105)	4010+2.0681	-
MS-RAAE+MLP	YES	0.96386 / (+/- 0.01201)	0.96387 / (+/- 0.01201)	0.96398 / (+/- 0.01185)	0.96386 / (+/- 0.01201)	4010+168.0656	-
MS-RAAE+GBC	YES	0.95701 / (+/- 0.01363)	0.95756 / (+/- 0.01251)	0.95718 / (+/- 0.01234)	0.95701 / (+/- 0.01297)	4010+29.8084	-
MS-RAAE+ABC	YES	0.89969 / (+/- 0.11173)	0.89748 / (+/- 0.11199)	0.90300/ (+/- 0.11150)	0.89969 / (+/- 0.11173)	4010+20.4527	-
MS-RAAE+CLF	YES	0.96636 / (+/- 0.01186)	0.96636 / (+/- 0.01186)	0.96636 / (+/- 0.01186)	0.96636 / (+/- 0.01186)	4010+221.9706	-

Table 3. Ablation results for the attention mechanism on the combined Figshare + Br35H + SARTAJ dataset

Metric Model	Pre-processing (Proposed method)	Accuracy/std	F1 Score/std	Precision/std	Sensitivity/std	Time(sec)	Total Number of Parameters
MS-GHOST-RAE	YES	0.96199	0.96215	0.96217	0.96199	3510	1329974
MS-GHOST-RAE+RF	YES	0.95452 / (+/- 0.01453)	0.95466 / (+/- 0.01453)	0.95494 / (+/- 0.01450)	0.95452 / (+/- 0.01453)	3510+1.799	-
MS-GHOST-RAE+SVM	YES	0.96449 / (+/- 0.01396)	0.96451 / (+/- 0.01394)	0.96468 / (+/- 0.01390)	0.96449 / (+/- 0.01396)	3510+0.4868	-
MS-GHOST-RAE+NB	YES	0.96449 / (+/- 0.01389)	0.96449 / (+/- 0.01389)	0.96449 / (+/- 0.01389)	0.96449 / (+/- 0.01389)	3510+0.3743	-
MS-GHOST-RAE+DT	YES	0.94268 / (+/- 0.01588)	0.94268 / (+/- 0.01588)	0.94268 / (+/- 0.01588)	0.94268 / (+/- 0.01588)	3510+8.8673	-
MS-GHOST-RAE+KNN	YES	0.94579 / (+/- 0.01834)	0.94605 / (+/- 0.01832)	0.94717 / (+/- 0.01831)	0.94579 / (+/- 0.01834)	3510+0.5912	-
MS-GHOST-RAE+LR	YES	0.96324 / (+/- 0.01482)	0.96323 / (+/- 0.01482)	0.96334 / (+/- 0.01481)	0.96324 / (+/- 0.01482)	3510+0.6980	-
MS-GHOST-RAE+MLP	YES	0.95576 / (+/- 0.00833)	0.99074 / (+/- 0.00833)	0.99074 / (+/- 0.00833)	0.99075 / (+/- 0.00833)	3510+131.6563	-
MS-GHOST-RAE+GBC	YES	0.95639 / (+/- 0.01516)	0.95638 / (+/- 0.01525)	0.95647 / (+/- 0.01542)	0.95639 / (+/- 0.01531)	3510+15.2492	-
MS-GHOST-RAE+ABC	YES	0.95389 / (+/- 0.10903)	0.95381 / (+/- 0.10903)	0.95383 / (+/- 0.10903)	0.95389 / (+/- 0.10903)	3510+14.1157	-
MS-GHOST-RAE+CLF	YES	0.95826 / (+/- 0.01701)	0.95826 / (+/- 0.01701)	0.95831 / (+/- 0.01701)	0.95826 / (+/- 0.01701)	3510+127.0532	-

Table 4. Ablation results for the residual blocks on the combined Figshare + Br35H + SARTAJ dataset

Metric Model	Pre-processing (Proposed method)	Accuracy/std	F1 Score/std	Precision/std	Sensitivity/std	Time(sec)	Total Number of Parameters
MS-GHOST-AAE	YES	0.97196	0.97216	0.97217	0.97196	3210	1388022
MS-GHOST-AAE+RF	YES	0.97321 / (+/- 0.01470)	0.97321 / (+/- 0.01470)	0.97321 / (+/- 0.01470)	0.97321 / (+/- 0.01470)	3210+2.6011	-
MS-GHOST-AAE+SVM	YES	0.97196 / (+/- 0.01145)	0.97194 / (+/- 0.01145)	0.97194 / (+/- 0.01145)	0.97196 / (+/- 0.01145)	3210+0.5898	-
MS-GHOST-AAE+NB	YES	0.97196 / (+/- 0.01321)	0.97202 / (+/- 0.0132)	0.97211 / (+/- 0.01325)	0.97196 / (+/- 0.01321)	3210+0.4131	-
MS-GHOST-AAE+DT	YES	0.96885 / (+/- 0.01416)	0.96877 / (+/- 0.01416)	0.96872 / (+/- 0.01416)	0.96885 / (+/- 0.01416)	3210+9.0329	-
MS-GHOST-AAE+KNN	YES	0.95826 / (+/- 0.01531)	0.95845 / (+/- 0.01531)	0.95912 / (+/- 0.01530)	0.95826 / (+/- 0.01531)	3210+0.6058	-
MS-GHOST-AAE+LR	YES	0.97196 / (+/- 0.01145)	0.97194 / (+/- 0.01145)	0.97194 / (+/- 0.01145)	0.97196 / (+/- 0.01145)	3210+1.3524	-
MS-GHOST-AAE+MLP	YES	0.97508 / (+/- 0.01120)	0.97509 / (+/- 0.01120)	0.97513 / (+/- 0.01120)	0.97508 / (+/- 0.01120)	3210+154.5673	-
MS-GHOST-AAE+GBC	YES	0.96885 / (+/- 0.01429)	0.96883 / (+/- 0.01429)	0.96882 / (+/- 0.01428)	0.96885 / (+/- 0.01429)	3210+24.8896	-
MS-GHOST-AAE+ABC	YES	0.97321 / (+/- 0.05822)	0.97335 / (+/- 0.05822)	0.97335 / (+/- 0.05820)	0.97321 / (+/- 0.05822)	3210+16.3706	-
MS-GHOST-AAE+CLF	YES	0.97570 / (+/- 0.01153)	0.97569 / (+/- 0.01154)	0.97572 / (+/- 0.01153)	0.97570 / (+/- 0.01153)	3210+197.0449	-

4.4. Performance Evaluation of The Proposed Hybrid Framework

This section reports the classification performance of the proposed MS-GHOST-RAAE-based hybrid framework on the combined Figshare + Br35H + SARTAJ dataset. The deep features extracted by MS-GHOST-RAAE were evaluated using different machine learning classifiers, including RF, SVM, NB, DT, KNN, LR, MLP, GBC, ABC, and CLF. The best classification performance was obtained with the MS-GHOST-RAAE-based hybrid configuration, achieving 98.75% accuracy with a total processing time of 543 + 269.4571 s.

4.5. Hyperparameter Sensitivity Analysis on The Combined Figshare + Br35H + SARTAJ Dataset

Three different experiments were conducted to examine the sensitivity of the proposed MS-GHOST-RAAE model to certain hyperparameters. These experiments were performed on the Figshare + Br35H + SARTAJ combined dataset. Three key components were investigated in the experiments: the pooling layer, the activation function, and the optimization algorithm. These components directly affect feature compression, the model's learning structure, and the progress of the training process. In the first experiment, the MaxPooling2D((2, 2)) layer used in the proposed model was replaced with AveragePooling2D((2, 2)). In the second experiment, the ELU activation function was used instead of the ReLU activation function. In the third experiment, the SGD algorithm was used instead of the Adam optimization algorithm. To ensure a fair comparison, other architectural settings were not changed. These experiments were only performed on the Figshare + Br35H + SARTAJ dataset because the study focused solely on the combined dataset.

Table 5. Hyperparameter sensitivity results for the pooling layer on the combined Figshare + Br35H + SARTAJ dataset

Metric Model	Pre-processing (Proposed method)	Accuracy/std	F1 Score/std	Precision/std	Sensitivity/std	Time(sec)	Total Number of Parameters
MS-GHOST-RAAE	YES	0.96449	0.96389	0.96396	0.96386	4110	1457782
MS-GHOST-RAAE+RF	YES	0.96075 / (+/- 0.01258)	0.96077 / (+/- 0.01250)	0.96082 / (+/- 0.01259)	0.96075 / (+/- 0.01258)	4110+3.0026	-
MS-GHOST-RAAE+SVM	YES	0.96386 / (+/- 0.01321)	0.96389 / (+/- 0.01318)	0.96399/ (+/- 0.01319)	0.96386/ (+/- 0.01321)	4110+0.4549	-
MS-GHOST-RAAE+NB	YES	0.96386 / (+/- 0.01304)	0.96400 / (+/- 0.01306)	0.96431 / (+/- 0.01299)	0.96386 / (+/- 0.01304)	4110+0.3945	-
MS-GHOST-RAAE+DT	YES	0.95327 / (+/- 0.01312)	0.95334 / (+/- 0.01312)	0.95343 / (+/- 0.01320)	0.95327 / (+/- 0.01312)	4110+9.0554	-
MS-GHOST-RAAE+KNN	YES	0.94704 / (+/- 0.01364)	0.94704 / (+/- 0.01364)	0.94793 / (+/- 0.01363)	0.94704 / (+/- 0.01364)	4110+0.8242	-
MS-GHOST-RAAE+LR	YES	0.96511 / (+/- 0.01240)	0.96514 / (+/- 0.01241)	0.96522 / (+/- 0.01240)	0.96511 / (+/- 0.01240)	4110+0.7313	-
MS-GHOST-RAAE+MLP	YES	0.96760 / (+/- 0.01032)	0.96765 / (+/- 0.01032)	0.96793 / (+/- 0.01035)	0.96760 / (+/- 0.01032)	4110+149.3096	-
MS-GHOST-RAAE+GBC	YES	0.95888 / (+/- 0.01535)	0.95887 / (+/- 0.01478)	0.95887 / (+/- 0.01561)	0.95888 / (+/- 0.01451)	4110+24.7205	-
MS-GHOST-RAAE+ABC	YES	0.80623 / (+/- 0.15215)	0.80666 / (+/- 0.15215)	0.80623 / (+/- 0.15215)	0.80623 / (+/- 0.15215)	4110+18.3785	-
MS-GHOST-RAAE+CLF	YES	0.96573 / (+/- 0.01297)	0.96568 / (+/- 0.01318)	0.96570 / (+/- 0.01318)	0.96573 / (+/- 0.01297)	4110+132.7330	-

Table 6. Hyperparameter sensitivity results for the activation function on the combined Figshare + Br35H + SARTAJ dataset

Metric Model	Pre-processing (Proposed method)	Accuracy/std	F1 Score/std	Precision/std	Sensitivity/std	Time(sec)	Total Number of Parameters
MS-GHOST-RAAE	YES	0.96199	0.96199	0.96120	0.96137	4410	1457782
MS-GHOST-RAAE+RF	YES	0.94704 / (+/- 0.01309)	0.94712 / (+/- 0.01309)	0.94723 / (+/- 0.01319)	0.94704 / (+/- 0.01309)	4410+2.6336	-
MS-GHOST-RAAE+SVM	YES	0.96137 / (+/- 0.01351)	0.96129 / (+/- 0.01355)	0.96125 / (+/- 0.01350)	0.96137 / (+/- 0.01351)	4410+0.4666	-
MS-GHOST-RAAE+NB	YES	0.95888 / (+/- 0.01345)	0.95890 / (+/- 0.01346)	0.95894 / (+/- 0.01346)	0.95888 / (+/- 0.01345)	4410+0.4250	-
MS-GHOST-RAAE+DT	YES	0.93333 / (+/- 0.01327)	0.93310 / (+/- 0.01327)	0.93298 / (+/- 0.01325)	0.93333 / (+/- 0.01327)	4410+8.0424	-
MS-GHOST-RAAE+KNN	YES	0.93084 / (+/- 0.01324)	0.93138 / (+/- 0.01324)	0.93272 / (+/- 0.01324)	0.93084 / (+/- 0.01324)	4410+0.6961	-
MS-GHOST-RAAE+LR	YES	0.96199 / (+/- 0.01321)	0.96188 / (+/- 0.01323)	0.96184 / (+/- 0.01321)	0.96199 / (+/- 0.01321)	4410+1.2843	-
MS-GHOST-RAAE+MLP	YES	0.95763 / (+/- 0.01286)	0.95763 / (+/- 0.01286)	0.95763 / (+/- 0.01286)	0.95763 / (+/- 0.01286)	4410+119.5911	-
MS-GHOST-RAAE+GBC	YES	0.93956 / (+/- 0.01394)	0.93946 / (+/- 0.01361)	0.93939 / (+/- 0.01371)	0.93956 / (+/- 0.01362)	4410+14.1525	-
MS-GHOST-RAAE+ABC	YES	0.79751 / (+/- 0.12549)	0.79736 / (+/- 0.12551)	0.79751 / (+/- 0.12549)	0.79751 / (+/- 0.12549)	4410+14.4993	-
MS-GHOST-RAAE+CLF	YES	0.95701 / (+/- 0.01309)	0.95689 / (+/- 0.01292)	0.95682 / (+/- 0.01309)	0.95701 / (+/- 0.01311)	4410+144.3441	-

Table 7. Hyperparameter sensitivity results for the optimizer on the combined Figshare + Br35H + SARTAJ dataset

Metric Model	Pre-processing (Proposed method)	Accuracy/std	F1 Score/std	Precision/std	Sensitivity/std	Time(sec)	Total Number of Parameters
MS-GHOST-RAAE	YES	0.95202	0.95117	0.95438	0.95202	4310	2416374
MS-GHOST-RAAE+RF	YES	0.96822 / (+/- 0.01391)	0.96827 / (+/- 0.01391)	0.96838 / (+/- 0.01379)	0.96822 / (+/- 0.01391)	4310+2.6464	-
MS-GHOST-RAAE+SVM	YES	0.95576 / (+/- 0.01452)	0.95518 / (+/- 0.01465)	0.95598 / (+/- 0.01452)	0.95576 / (+/- 0.01452)	4310+0.5072	-
MS-GHOST-RAAE+NB	YES	0.96324 / (+/- 0.01344)	0.96324 / (+/- 0.01344)	0.96324 / (+/- 0.01344)	0.96324 / (+/- 0.01344)	4310+0.4389	-
MS-GHOST-RAAE+DT	YES	0.95265 / (+/- 0.01427)	0.95259 / (+/- 0.01427)	0.95261 / (+/- 0.01428)	0.95265 / (+/- 0.01427)	4310+8.0297	-
MS-GHOST-RAAE+KNN	YES	0.95265 / (+/- 0.01464)	0.95284 / (+/- 0.01450)	0.95270 / (+/- 0.01464)	0.95265 / (+/- 0.01464)	4310+0.6213	-
MS-GHOST-RAAE+LR	YES	0.95452 / (+/- 0.01364)	0.95387 / (+/- 0.01372)	0.95635 / (+/- 0.01360)	0.95452 / (+/- 0.01364)	4310+0.9021	-
MS-GHOST-RAAE+MLP	YES	0.96636 / (+/- 0.01156)	0.96636 / (+/- 0.01156)	0.96636 / (+/- 0.01156)	0.96636 / (+/- 0.01156)	4310+107.9024	-
MS-GHOST-RAAE+GBC	YES	0.96137 / (+/- 0.01273)	0.96146 / (+/- 0.01274)	0.96159 / (+/- 0.01273)	0.96137 / (+/- 0.01293)	4310+15.8251	-
MS-GHOST-RAAE+ABC	YES	0.73894 / (+/- 0.11536)	0.73894 / (+/- 0.11536)	0.73894 / (+/- 0.11536)	0.73894 / (+/- 0.11536)	4310+12.8045	-
MS-GHOST-RAAE+CLF	YES	0.96636 / (+/- 0.01324)	0.96633 / (+/- 0.01358)	0.96639 / (+/- 0.01351)	0.96636 / (+/- 0.01333)	4310+138.0432	-

Tables 5–7 present the results of hyperparameter sensitivity analyses performed on a combined dataset generated from Figshare + Br35H + SARTAJ sources. The findings show that the original configuration of the proposed MS-GHOST-RAAE model is the most successful setup with an accuracy of 98.75%. The decrease in performance when replacing the MaxPooling2D layer with AveragePooling2D can be attributed to the fact that average pooling produces smoother and less detailed feature maps. This suggests that MaxPooling2D is more suitable for the proposed architecture in terms of preserving distinct local features associated with tumors.

In the activation function experiments, ELU was used instead of ReLU. This change reduced the classification success in the combined dataset. ELU can improve gradient flow in some cases. However, ReLU yielded more suitable results for the heterogeneous MRI images in this study. ReLU provided a simpler, more stable, and more effective nonlinear transformation. Similarly, SGD was used instead of Adam in the optimization experiments. The use of SGD reduced the overall classification performance. This result shows that the Adam algorithm is more successful for the proposed model. Especially when considering the variability in the combined dataset from different sources, the Adam optimization algorithm optimized the model more effectively.

Overall, hyperparameter sensitivity analysis confirms that the original MS-GHOST-RAAE configuration, including MaxPooling2D, ReLU activation, and the Adam optimization algorithm, offers the strongest classification performance

on the combined Figshare + Br35H + SARTAJ dataset. Therefore, this configuration has been retained as the final model setting in the proposed framework.

4.6. Performance comparison with machine learning classifiers on the combined dataset

The results presented in Tables 8–12 demonstrate that the proposed image processing and hybrid learning framework provides higher classification performance compared to the transfer learning-based baseline models evaluated on the combined Figshare + Br35H + SARTAJ dataset.

Overall, these tables reveal that the MS-GHOST-RAAE-based hybrid approach is more effective than the associated transfer learning models. Although ResNet-based models produce stronger results than VGG16 due to their residual learning structures, none of the evaluated transfer learning architectures reached the classification performance achieved by the proposed method. The superior performance of MS-GHOST-RAAE stems from the combined use of tumor-focused preprocessing steps, wavelet-based enhancement, multi-scale GHOST feature extraction, information flow supported by residual connections, and feature enhancement based on attention mechanisms. These findings confirm that the proposed framework offers a more suitable and effective solution for heterogeneous multi-class brain tumor MRI classification compared to traditional transfer learning-based approaches.

Table 8. Performance metrics of the proposed MS-GHOST-RAAE-based hybrid framework on the combined Figshare + Br35H + SARTAJ dataset

Metric Model	Pre-processing (Proposed method)	Accuracy/std	F1 Score/std	Precision/std	Sensitivity/std	Time(sec)	Total Number of Parameters
MS-GHOST-RAAE	YES	0.98692	0.98692	0.98692	0.98692	543	2416374
MS-GHOST-RAAE+RF	YES	0.98505 / (+/- 0.00873)	0.98505 / (+/- 0.00873)	0.98505 / (+/- 0.00873)	0.98505 / (+/- 0.00873)	543+3.0079	-
MS-GHOST-RAAE+SVM	YES	0.98692 / (+/- 0.00903)	0.98692 / (+/- 0.00903)	0.98692 / (+/- 0.00903)	0.98692 / (+/- 0.00903)	543+0.7518	-
MS-GHOST-RAAE+NB	YES	0.98692 / (+/- 0.00924)	0.98692 / (+/- 0.00924)	0.98692 / (+/- 0.00924)	0.98692 / (+/- 0.00924)	543+0.3445	-
MS-GHOST-RAAE+DT	YES	0.98006 / (+/- 0.00970)	0.98006 / (+/- 0.00970)	0.98006 / (+/- 0.00970)	0.98006 / (+/- 0.00970)	543+7.0357	-
MS-GHOST-RAAE+KNN	YES	0.98193 / (+/- 0.01042)	0.98193 / (+/- 0.01042)	0.98193 / (+/- 0.01042)	0.98193 / (+/- 0.01042)	543+0.5478	-
MS-GHOST-RAAE+LR	YES	0.98692 / (+/- 0.01035)	0.98692 / (+/- 0.01035)	0.98692 / (+/- 0.01035)	0.98692 / (+/- 0.01035)	543+0.9777	-
MS-GHOST-RAAE+MLP	YES	0.98754 / (+/- 0.00901)	0.98754 / (+/- 0.00901)	0.98754 / (+/- 0.00901)	0.98754 / (+/- 0.00901)	543+269.4571	-
MS-GHOST-RAAE+GBC	YES	0.98442 / (+/- 0.00799)	0.98442 / (+/- 0.00816)	0.98447 / (+/- 0.00790)	0.98442 / (+/- 0.00790)	543+15.5354	-
MS-GHOST-RAAE+ABC	YES	0.68723 / (+/- 0.12138)	0.68723 / (+/- 0.12138)	0.68723 / (+/- 0.12138)	0.68723 / (+/- 0.12138)	543+14.2489	-
MS-GHOST-RAAE+CLF	YES	0.98692 / (+/- 0.00818)	0.98692 / (+/- 0.00818)	0.98692 / (+/- 0.00818)	0.98692 / (+/- 0.00818)	543+108.9838	-

Table 9. ResNet50V2 performance measurements on the combined Figshare + Br35H + SARTAJ dataset

Metric Model	Pre-processing (Proposed method)	Accuracy/std	F1 Score/std	Precision/std	Sensitivity/std	Time(sec)	Total Number of Parameters
ResNet50V2	YES	0.93831	0.93836	0.93907	0.93831	374	23572996
ResNet50V2+RF	YES	0.92461 / (+/- 0.02049)	0.92461 / (+/- 0.02049)	0.92461 / (+/- 0.02049)	0.92461 / (+/- 0.02049)	248+3.2145	-
ResNet50V2+SVM	YES	0.94019 / (+/- 0.01833)	0.94019 / (+/- 0.01833)	0.94019 / (+/- 0.01833)	0.94019 / (+/- 0.01833)	248+0.5757	-
ResNet50V2+NB	YES	0.92960 / (+/- 0.01945)	0.92960 / (+/- 0.01945)	0.92960 / (+/- 0.01945)	0.92960 / (+/- 0.01945)	248+0.3589	-
ResNet50V2+DT	YES	0.90530 / (+/- 0.02222)	0.90530 / (+/- 0.02222)	0.90530 / (+/- 0.02222)	0.90530 / (+/- 0.02222)	248+7.4952	-
ResNet50V2+KNN	YES	0.89408 / (+/- 0.02822)	0.89408 / (+/- 0.02822)	0.89408 / (+/- 0.02822)	0.89408 / (+/- 0.02822)	248+0.6036	-
ResNet50V2+LR	YES	0.93832 / (+/- 0.01816)	0.93832 / (+/- 0.01816)	0.93832 / (+/- 0.01816)	0.93832 / (+/- 0.01816)	248+0.9861	-
ResNet50V2+MLP	YES	0.93209 / (+/- 0.01946)	0.93209 / (+/- 0.01946)	0.93209 / (+/- 0.01946)	0.93209 / (+/- 0.01946)	248+242.4685	-
ResNet50V2+GBC	YES	0.92461/ (+/- 0.01938)	0.92451 / (+/- 0.01838)	0.92453 / (+/- 0.01943)	0.92149 / (+/- 0.01917)	248+36.6612	-
ResNet50V2+ABC	YES	0.69034 / (+/- 0.06463)	0.69034 / (+/- 0.06463)	0.69034 / (+/- 0.06463)	0.69034 / (+/- 0.06463)	248+14.4663	-
ResNet50V2+CLF	YES	0.93271 / (+/- 0.02064)	0.93271 / (+/- 0.02064)	0.93271 / (+/- 0.02064)	0.93271 / (+/- 0.02064)	248+204.7089	-

Table 10. ResNet101 performance measurements on the combined Figshare + Br35H + SARTAJ dataset

Metric Model	Pre-processing (Proposed method)	Accuracy/std	F1 Score/std	Precision/std	Sensitivity/std	Time(sec)	Total Number of Parameters
ResNet101V2	YES	0.94704	0.94697	0.94696	0.94704	490	42634756
ResNet101V2+RF	YES	0.93894 / (+/- 0.02077)	0.93894 / (+/- 0.02077)	0.93894 / (+/- 0.02077)	0.93894 / (+/- 0.02077)	490+4.2447	-
ResNet101V2+SVM	YES	0.94704 / (+/- 0.02203)	0.94704 / (+/- 0.02203)	0.94704 / (+/- 0.02203)	0.94704 / (+/- 0.02203)	490+0.5687	-
ResNet101V2+NB	YES	0.94393 / (+/- 0.02041)	0.94393 / (+/- 0.02041)	0.94393 / (+/- 0.02041)	0.94393 / (+/- 0.02041)	490+0.5489	-
ResNet101V2+DT	YES	0.90966 / (+/- 0.02049)	0.90966 / (+/- 0.02049)	0.90966 / (+/- 0.02049)	0.90966 / (+/- 0.02049)	490+8.0706	-
ResNet101V2+KNN	YES	0.91340 / (+/- 0.01947)	0.91340 / (+/- 0.01947)	0.91340 / (+/- 0.01947)	0.91340 / (+/- 0.01947)	490+0.5778	-
ResNet101V2+LR	YES	0.94704 / (+/- 0.02275)	0.94704 / (+/- 0.02275)	0.94704 / (+/- 0.02275)	0.94704 / (+/- 0.02275)	490+1.3948	-
ResNet101V2+MLP	YES	0.94393 / (+/- 0.02132)	0.94393 / (+/- 0.02132)	0.94393 / (+/- 0.02132)	0.94393 / (+/- 0.02132)	490+242.3883	-
ResNet101V2+GBC	YES	0.93583 / (+/- 0.01961)	0.93620 / (+/- 0.02076)	0.93693 / (+/- 0.01965)	0.93583 / (+/- 0.02000)	490+24.2785	-
ResNet101V2+ABC	YES	0.75888 / (+/- 0.08343)	0.76814 / (+/- 0.08810)	0.78476 / (+/- 0.08815)	0.75888 / (+/- 0.08810)	490+18.6103	-
ResNet101V2+CLF	YES	0.94393 / (+/- 0.02223)	0.94393 / (+/- 0.02223)	0.94393 / (+/- 0.02223)	0.94393 / (+/- 0.02223)	490+211.1037	-

Table 11. ResNet152 performance measurements on the combined Figshare + Br35H + SARTAJ dataset

Metric Model	Pre-processing (Proposed method)	Accuracy/std	F1 Score/std	Precision/std	Sensitivity/std	Time(sec)	Total Number of Parameters
ResNet152V2	YES	0.93644	0.93588	0.93592	0.93644	955	58339844
ResNet152V2+RF	YES	0.93520 / (+/- 0.01674)	0.93520 / (+/- 0.01674)	0.93520 / (+/- 0.01674)	0.93520 / (+/- 0.01674)	955+3.1788	-
ResNet152V2+SVM	YES	0.93832 / (+/- 0.01729)	0.93781 / (+/- 0.01729)	0.93773 / (+/- 0.01729)	0.93832 / (+/- 0.01729)	955+0.6322	-
ResNet152V2+NB	YES	0.93583 / (+/- 0.01621)	0.93571 / (+/- 0.01600)	0.93564 / (+/- 0.01643)	0.93583 / (+/- 0.01621)	955+1.15120	-
ResNet152V2+DT	YES	0.91402 / (+/- 0.02426)	0.91402 / (+/- 0.02426)	0.91402 / (+/- 0.02426)	0.91402 / (+/- 0.02426)	955+6.9344	-
ResNet152V2+KNN	YES	0.89470 / (+/- 0.02180)	0.89506 / (+/- 0.02100)	0.89842 / (+/- 0.02095)	0.89470 / (+/- 0.02180)	955+0.5161	-
ResNet152V2+LR	YES	0.93832 / (+/- 0.01783)	0.93832 / (+/- 0.01783)	0.93832 / (+/- 0.01783)	0.93832 / (+/- 0.01783)	955+1.3488	-
ResNet152V2+MLP	YES	0.93769 / (+/- 0.01806)	0.93747 / (+/- 0.01726)	0.93735 / (+/- 0.01710)	0.93769 / (+/- 0.01806)	955+216.5901	-
ResNet152V2+GBC	YES	0.92960 / (+/- 0.01834)	0.92928 / (+/- 0.01770)	0.92911 / (+/- 0.01780)	0.92960 / (+/- 0.01754)	955+23.3878	-
ResNet152V2+ABC	YES	0.90530 / (+/- 0.03783)	0.90530 / (+/- 0.03783)	0.90530 / (+/- 0.03783)	0.90530 / (+/- 0.03783)	955+14.0761	-
ResNet152V2+CLF	YES	0.93832 / (+/- 0.01718)	0.93832 / (+/- 0.01718)	0.93832 / (+/- 0.01718)	0.93832 / (+/- 0.01718)	955+207.6112	-

Table 12. VGG16 performance measurements on the combined Figshare + Br35H + SARTAJ dataset

Metric Model	Pre-processing (Proposed method)	Accuracy/std	F1 Score/std	Precision/std	Sensitivity/std	Time(sec)	Total Number of Parameters
VGG16	YES	0.88224	0.88333	0.88521	0.88224	469	14716740
VGG16+RF	YES	0.87788 / (+/- 0.02051)	0.87788 / (+/- 0.02051)	0.87788 / (+/- 0.02051)	0.87788 / (+/- 0.02051)	469+4.3178	-
VGG16+SVM	YES	0.88972 / (+/- 0.02506)	0.88978 / (+/- 0.02506)	0.89072 / (+/- 0.02506)	0.88972 / (+/- 0.02506)	469+1.4788	-
VGG16+NB	YES	0.88224 / (+/- 0.02569)	0.88224 / (+/- 0.02569)	0.88224 / (+/- 0.02569)	0.88224 / (+/- 0.02569)	469+0.3496	-
VGG16+DT	YES	0.84735 / (+/- 0.02126)	0.84735 / (+/- 0.02126)	0.84735 / (+/- 0.02126)	0.84735 / (+/- 0.02126)	469+6.7846	-
VGG16+KNN	YES	0.82866 / (+/- 0.02314)	0.83067 / (+/- 0.02310)	0.83665 / (+/- 0.02328)	0.82866 / (+/- 0.02314)	469+0.4069	-
VGG16+LR	YES	0.89097 / (+/- 0.02543)	0.89097 / (+/- 0.02543)	0.89097 / (+/- 0.02543)	0.89097 / (+/- 0.02543)	469+0.4268	-
VGG16+MLP	YES	0.89221 / (+/- 0.02374)	0.89212 /(+/- 0.02383)	0.89419 / (+/- 0.02360)	0.89221 / (+/- 0.02374)	469+236.7502	-
VGG16+GBC	YES	0.88162 / (+/- 0.02097)	0.88095 / (+/- 0.02075)	0.88111 / (+/- 0.02149)	0.88162 / (+/- 0.02098)	469+23.2962	-
VGG16+ABC	YES	0.61869 / (+/- 0.10957)	0.61869 / (+/- 0.10957)	0.61869 / (+/- 0.10957)	0.61869 / (+/- 0.10957)	469+14.2217	-
VGG16+CLF	YES	0.88349 / (+/- 0.02096)	0.88291 / (+/- 0.02136)	0.88310 / (+/- 0.02130)	0.88349 / (+/- 0.02096)	469+600. 1049	-

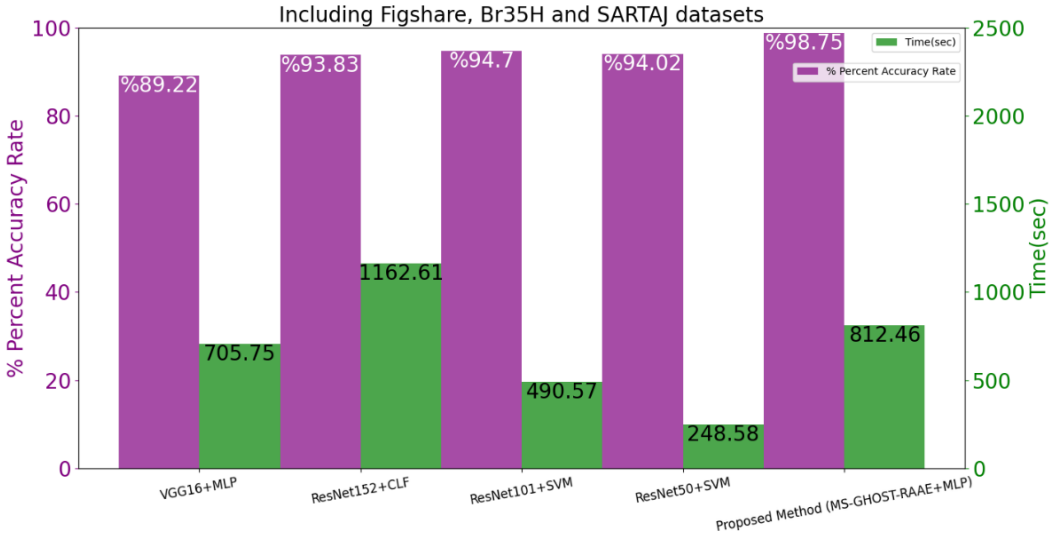

Figure 12. Comparison of the accuracy metrics of our proposed method with modern transfer-learning algorithms for the (Including Figshare, Br35H, and SARTAJ datasets) image dataset

Fig. 12 presents the accuracy and computation time results of different hybrid deep learning models evaluated on a combined dataset created from Figshare, Br35H, and SARTAJ sources. The VGG16+MLP model produced the lowest accuracy value at 89.22%, while all ResNet-based configurations achieved accuracy above 93%, demonstrating stronger feature extraction capabilities on heterogeneous data structures. The proposed MS-GHOST-RAAE+MLP method achieved the highest classification performance on the combined dataset, reaching an accuracy rate of 98.75%. Although the processing time was moderate compared to other models, the significant increase in prediction accuracy reveals that the proposed architecture is an effective approach for large and diverse MRI data collections. The results show that the MS-GHOST-RAAE-based hybrid framework offers higher classification performance compared to transfer learning-based models evaluated on the combined Figshare + Br35H + SARTAJ dataset. This performance increase is due to; The study demonstrates that the combined use of specialized preprocessing steps, wavelet transform, multi-scale GHOST feature extraction, residual learning associations, attentional mechanisms, and machine learning-based classification contributes to obtaining more distinctive representations from heterogeneous MRI images.

4.7. Loss, Accuracy Graphics and Confusion Matrix Of Analysis Results

Fig. 13 shows the training and validation results of the proposed MS-GHOST-RAAE model. These results were obtained on the Figshare + Br35H + SARTAJ combined dataset. The training and validation curves are given in the figure. These curves show that the model learned stably. Confusion matrix results are also presented. The complexity matrices show the model's success in distinguishing four classes. These classes are glioma, meningioma, no-tumor, and pituitary tumor. In the confusion matrix, 0 represents the glioma class, 1 represents the meningioma class, 2 represents the no-tumor class, and 3 represents the pituitary tumor class.

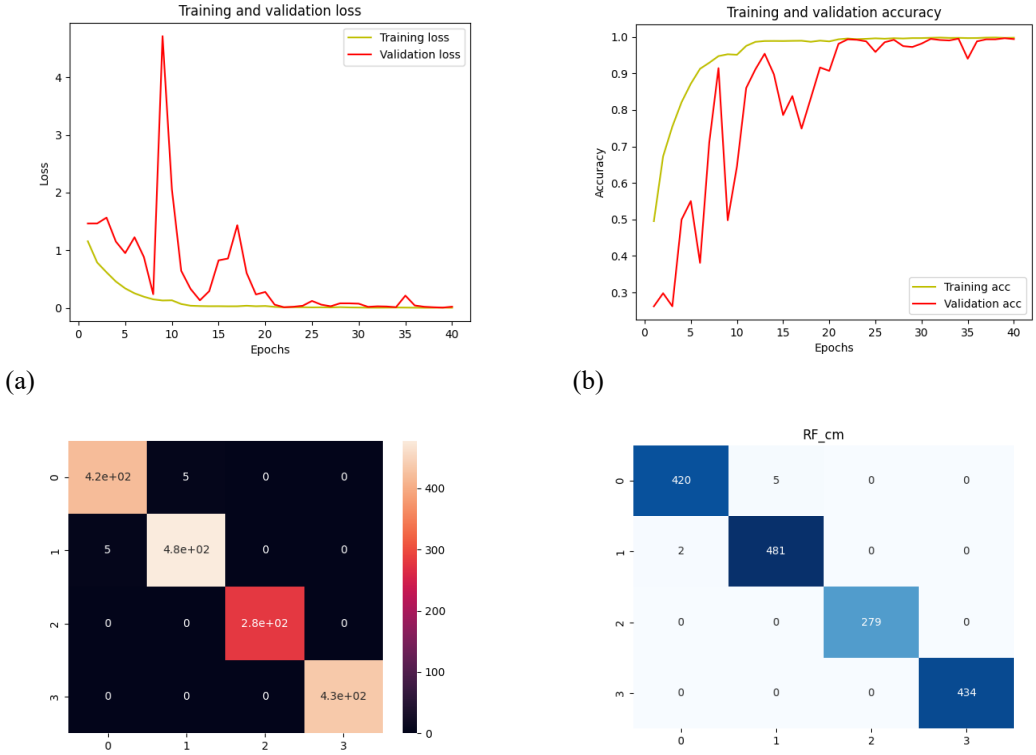

Figure 13. Training curves and confusion matrix results of the proposed MS-GHOST-RAAE model on the combined Figshare + Br35H + SARTAJ dataset.

The confusion matrix results support the numerical performance values obtained by the proposed MS-GHOST-RAAE + MLP model. Most MRI images were classified into their correct classes, which shows that the model can effectively distinguish glioma, meningioma, no-tumor, and pituitary tumor categories. In addition to the 98.75% accuracy value, the high F1-score, precision, and sensitivity values indicate that the model provides balanced classification performance. High precision means that false positive predictions are limited, while high sensitivity means that most actual tumor samples are correctly detected. This is especially important in medical image classification, where false negative predictions may cause serious clinical risks. Therefore, the proposed framework demonstrates reliable performance not only in terms of accuracy but also in terms of clinically meaningful evaluation metrics.

Table 13. Comparison of the proposed MS-GHOST-RAAE-based hybrid framework with the related study using the combined Figshare + Br35H + SARTAJ dataset

Reference	Method	Image pre-processing	Dataset	Accuracy (%)	Classification
[27]	CNN + DT, NB, KNN, SVM	No	Including Figshare + Br35H + SARTAJ	97.93	Multiclass
Proposed Method	MS-GHOST-RAAE + ML classifiers	Yes	Combined Figshare + Br35H + SARTAJ	98.75	Multiclass

Table 13 compares the proposed MS-GHOST-RAAE-based hybrid framework with the related study [27] using the same combined Figshare + Br35H + SARTAJ dataset. The reference study employed CNN-based feature extraction with conventional machine learning classifiers, including DT, NB, KNN, and SVM, and achieved 97.93% accuracy without applying a dedicated image preprocessing stage. In contrast, the proposed method integrates a comprehensive preprocessing pipeline, wavelet transformation, multi-scale GHOST feature extraction, residual learning, attention mechanism, and machine learning-based classification. As a result, the proposed framework achieved a higher classification accuracy of 98.75% on the same multiclass MRI dataset. This improvement indicates that the proposed MS-GHOST-RAAE-based feature representation provides more discriminative and robust information for heterogeneous brain tumor MRI classification. Therefore, the comparison confirms that the proposed framework not only improves classification performance over the directly comparable study but also provides a more systematic and tumor-oriented feature extraction strategy for multi-source MRI data.

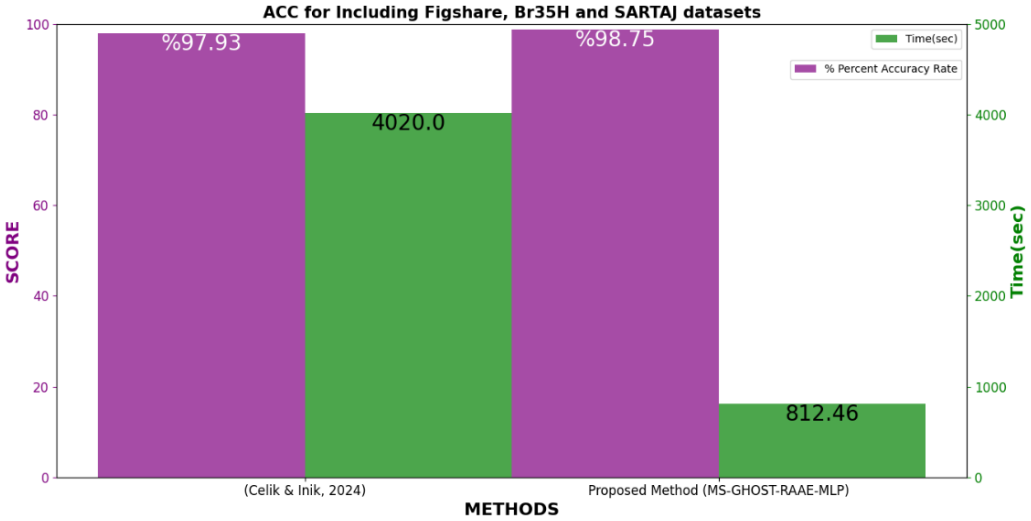

Figure 14. Accuracy and computational time comparison with the related study using the combined Figshare + Br35H + SARTAJ dataset.

Fig. 14 compares the performance of the proposed MS-GHOST-RAAE-MLP model with the method reported by Celik and Inik (2024) [27] on the combined Figshare, Br35H, and SARTAJ dataset. Although the reference method achieves a high accuracy of 97.93%, its computational time exceeds 4000 s. In contrast, the proposed model attains a higher accuracy of 98.75% while completing the task in 812.46 s. These results indicate that the proposed framework improves both classification accuracy and computational efficiency on the heterogeneous combined MRI dataset.

In this study, Figshare, Br35H, and SARTAJ datasets were combined. This combined dataset was used to evaluate the proposed image processing and hybrid learning method. The proposed MS-GHOST-RAAE-MLP structure achieved the highest classification success, reaching an accuracy rate of 98.75%. Model success was not evaluated solely by accuracy. F1-score, precision, sensitivity, complexity matrices, and loss-of-accuracy curves were also used. These results demonstrate that the proposed method successfully distinguishes between glioma, meningioma, non-tumor, and pituitary tumor classes. To improve the reliability of the final classification stage, 10-fold cross-validation was applied to the machine learning classifiers. A comparison was made with a related study using the same combined dataset. This comparison showed that the proposed method provided higher performance. This success stems from the combined use of appropriate preprocessing, wavelet transform, MS-GHOST-RAAE-based feature extraction, and machine learning-based classification. These components contribute to obtaining cleaner and more distinctive features from heterogeneous MRI images.

The obtained results also show the advantage of evaluating the proposed method on a multi-source heterogeneous MRI dataset. Since the combined Figshare–Br35H–SARTAJ dataset contains images from different sources, it includes higher visual variability than a single-source dataset. This variability makes the classification problem more difficult. However, the proposed MS-GHOST-RAAE framework achieved strong classification performance under this heterogeneous setting. This indicates that the proposed preprocessing, wavelet transformation, GHOST-based feature extraction, residual learning, and attention refinement steps can produce robust and discriminative features for MRI images with different visual characteristics.

5. Conclusion

This study proposes a hybrid brain tumor MRI classification method based on MS-GHOST-RAAE. This method utilizes a combination of deep feature extraction and machine learning classifiers. Experiments were conducted on a dataset created by combining Figshare, Br35H, and SARTAJ datasets. This dataset includes four classes: glioma, meningioma, no-tumor, and pituitary tumor. The combined dataset, composed of data from different sources, presents a more challenging and realistic evaluation environment. The proposed preprocessing steps utilize grayscale transformation, Otsu thresholding, region of interest extraction, color-based segmentation, masking, Canny edge detection, contour detection, and wavelet transformation. These steps make tumor-related regions more prominent. Subsequently, short and distinctive deep features are extracted using the MS-GHOST-RAAE architecture. This architecture combines multi-scale GHOST modules, residual connections, and attention mechanisms. The extracted features are classified using traditional machine learning methods. According to experimental results, the proposed hybrid method achieved 98.75% accuracy on the combined dataset. The total processing time was measured as 543 + 269.4571 seconds. Ablation experiments showed that the GHOST mechanism, the attention mechanism, and residual connections contributed to the model's success. Furthermore, hyperparameter analysis revealed that the original configuration using MaxPooling2D, ReLU, and the Adam optimization algorithm yielded the best results. Overall, the proposed MS-GHOST-RAAE-based hybrid method offers an accurate and feasible solution for multi-class brain tumor classification in MRI images from diverse sources. Future

studies could test this method with larger patient groups, different hospital datasets, and explainable artificial intelligence methods.

Declarations Conflict of interest The authors declared that they have no conflicts of interest in this work.

Acknowledgments
The authors would like to acknowledge Masoud Nickparvar for publicly providing the Brain Tumor MRI Dataset through the Kaggle platform, which was used in this study. The dataset was accessed on March 3, 2021.

References

[1]. Abirami, S., & Prasanna Venkatesan, D. G. K. D. (2022). Deep learning and spark architecture based intelligent brain tumor MRI image severity classification. *Biomedical Signal Processing and Control*, *76*, 103644. https://doi.org/10.1016/j.bspc.2022.103644

[2]. Arı, A., & Hanbay, D. (2018). Deep learning based brain tumor classification and detection system. *Turkish Journal of Electrical Engineering and Computer Sciences*, *26*(5), 2275–2286. https://doi.org/10.3906/elk-1801-8

[3]. Operto, F. F., Pastorino, G. M. G., Stellato, M., Morcaldi, L., Vetri, L., Carotenuto, M., Viggiano, A., & Coppola, G. (2020). Facial emotion recognition in children and adolescents with specific learning disorder. *Brain Sciences*, *10*(8), 473. https://doi.org/10.3390/brainsci10080473

[4]. Sajid, S., Hussain, S., & Sarwar, A. (2019). Brain tumor detection and segmentation in MR images using deep learning. *Arabian Journal for Science and Engineering*, *44*(11), 9249–9261. https://doi.org/10.1007/s13369-019-03967-8

[5]. Cheng, J., Huang, W., Cao, S., Yang, R., Yang, W., Yun, Z., Wang, Z., & Feng, Q. (2015). Enhanced performance of brain tumor classification via tumor region augmentation and partition. *PLOS ONE*, *10*(10), e0140381. https://doi.org/10.1371/journal.pone.0140381

[6]. Michael Mahesh, K., & Arokia Renjit, J. (2020). Multiclassifier for severity-level categorization of glioma tumors using multimodal magnetic resonance imaging brain images. *International Journal of Imaging Systems and Technology*, *30*(1), 234–251. https://doi.org/10.1002/ima.22357

[7]. Zhou, Y., Li, Z., Zhu, H., Chen, C., Gao, M., Xu, K., & Xu, J. (2019). Holistic brain tumor screening and classification based on denseNet and recurrent neural network. In A. Crimi, S. Bakas, H. Kuijf, F. Keyvan, M. Reyes, & T. van Walsum (Eds.), *Brainlesion: Glioma, Multiple Sclerosis, Stroke and Traumatic Brain Injuries. BrainLes 2018* (pp. 208–217). https://doi.org/10.1007/978-3-030-11723-8_21

[8]. El-Dahshan, E.-S. A., Mohsen, H. M., Revett, K., & Salem, A.-B. M. (2014). Computer-aided diagnosis of human brain tumor through MRI: A survey and a new algorithm. *Expert Systems with Applications*, *41*(11), 5526–5545. https://doi.org/10.1016/j.eswa.2014.01.021

[9]. Kanmani, P., & Marikkannu, P. (2018). MRI brain images classification: A multi-level threshold based region optimization technique. *Journal of Medical Systems*, *42*(4), 62. https://doi.org/10.1007/s10916-018-0915-8

[10]. Oliva, J. B., Dubey, A., Zaheer, M., Póczos, B., Salakhutdinov, R., Xing, E. P., & Schneider, J. (2018). Transformation autoregressive networks. *Proceedings of the 35th International Conference on Machine Learning*, 3898–3907. https://proceedings.mlr.press/v80/oliva18a.html

[11]. Talo, M., Baloglu, U. B., Yıldırım, Ö., & Rajendra Acharya, U. (2019). Application of deep transfer learning for automated brain abnormality classification using MR images. *Cognitive Systems Research*, *54*, 176–188. https://doi.org/10.1016/j.cogsys.2018.12.007

[12]. van den Oord, A., Kalchbrenner, N., Espeholt, L., kavukcuoglu, koray, Vinyals, O., & Graves, A. (2016). Conditional image generation with pixelCNN decoders. In D. Lee, M. Sugiyama, U. Luxburg, I. Guyon, & R. Garnett (Eds.), *Advances in Neural Information Processing Systems* (Vol. 29). Curran Associates, Inc. https://proceedings.neurips.cc/paper_files/paper/2016/file/b1301141feffabac455e1f90a7de2054-Paper.pdf

[13]. Tiwari, A., Srivastava, S., & Pant, M. (2020). Brain tumor segmentation and classification from magnetic resonance images: Review of selected methods from 2014 to 2019. *Pattern Recognition Letters*, *131*, 244–260. https://doi.org/10.1016/j.patrec.2019.11.020

[14]. Kuzman, B., Petković, B., Denić, N., Petković, D., Ćirković, B., Stojanović, J., & Milić, M. (2021). Estimation of optimal fertilizers for optimal crop yield by adaptive neuro fuzzy logic. *Rhizosphere*, *18*, 100358. https://doi.org/10.1016/j.rhisph.2021.100358

[15]. Milić, M., Petković, B., Selmi, A., Petković, D., Jermsittiparsert, K., Radivojević, A., Milovancevic, M., Khan, A., Vidosavljević, S. T., Denić, N., & Kuzman, B. (2023). Computational evaluation of microalgae biomass conversion to biodiesel. *Biomass Conversion and Biorefinery*, *13*(4), 3179–3186. https://doi.org/10.1007/s13399-021-01314-2

[16]. Milićević, V., Denić, N., Milićević, Z., Arsić, L., Spasić-Stojković, M., Petković, D., Stojanović, J., Krkic, M., Milovančević, N. S., & Jovanović, A. (2021). E-learning perspectives in higher education institutions. *Technological Forecasting and Social Change*, *166*, 120618. https://doi.org/10.1016/j.techfore.2021.120618

[17]. Petković, D., Barjaktarovic, M., Milošević, S., Denić, N., Spasić, B., Stojanović, J., & Milovancevic, M. (2021). Neuro fuzzy estimation of the most influential parameters for Kusum biodiesel performance. *Energy*, *229*, 120621. https://doi.org/10.1016/j.energy.2021.120621

[18]. Stojanović, J., Petkovic, D., Alarifi, I. M., Cao, Y., Denic, N., Ilic, J., Assilzadeh, H., Resic, S., Petkovic, B., Khan, A., & Milickovic, M. (2021). Application of distance learning in mathematics through adaptive neuro-fuzzy learning method. *Computers & Electrical Engineering*, *93*, 107270. https://doi.org/10.1016/j.compeleceng.2021.107270

[19]. Alqazzaz, S., Sun, X., Yang, X., & Nokes, L. (2019). Automated brain tumor segmentation on multi-modal MR image using SegNet. *Computational Visual Media*, *5*(2), 209–219. https://doi.org/10.1007/s41095-019-0139-y

[20]. Kamnitsas, K., Ledig, C., Newcombe, V. F. J., Simpson, J. P., Kane, A. D., Menon, D. K., Rueckert, D., & Glocker, B. (2017). Efficient multi-scale 3D CNN with fully connected CRF for accurate brain lesion segmentation. *Medical Image Analysis*, *36*, 61–78. https://doi.org/10.1016/j.media.2016.10.004

[21]. Srinivas, V., & Santhirani, C. (2020). Hybrid particle swarm optimization-deep neural network model for speaker recognition. *Multimedia Research*, *3*(1), 1. https://doi.org/10.46253/j.mr.v3i1.a1

[22]. Kaldera, H. N. T. K., Gunasekara, S. R., & Dissanayake, M. B. (2019). Brain tumor classification and segmentation using faster R-CNN. *2019 Advances in Science and Engineering Technology International Conferences (ASET)*, 1–6. https://doi.org/10.1109/ICASET.2019.8714263

[23]. Bernal, J., Kushibar, K., Asfaw, D. S., Valverde, S., Oliver, A., Martí, R., & Lladó, X. (2019). Deep convolutional neural networks for brain image analysis on magnetic resonance imaging: A review. *Artificial Intelligence in Medicine*, *95*, 64–81. https://doi.org/10.1016/j.artmed.2018.08.008

[24]. Seetha, J., & Raja, S. S. (2018). Brain tumor classification using convolutional neural networks. *Biomedical and Pharmacology Journal*, *11*(3), 1457–1461. https://doi.org/10.13005/bpj/1511

[25]. Ismail, M., Soliman, A., Ghazal, M., Switala, A. E., Gimel'farb, G., Barnes, G. N., Khalil, A., & El-Baz, A. (2017). A fast stochastic framework for automatic MR brain images segmentation. *PLOS ONE*, *12*(11), e0187391. https://doi.org/10.1371/journal.pone.0187391

[26]. Tandel, G. S., Biswas, M., Kakde, O. G., Tiwari, A., Suri, H. S., Turk, M., Laird, J., Asare, C., Ankrah, A. A., Khanna, N. N., Madhusudhan, B. K., Saba, L., & Suri, J. S. (2019). A review on a deep learning perspective in brain cancer classification. *Cancers*, *11*(1), 111. https://doi.org/10.3390/cancers11010111

[27]. Celik, M., & Inik, O. (2024). Development of hybrid models based on deep learning and optimized machine learning algorithms for brain tumor multi-classification. *Expert Systems with Applications*, *238*, 122159. https://doi.org/10.1016/j.eswa.2023.122159

[28]. Abbas, Q., Fondón, I., & Rashid, M. (2011). Unsupervised skin lesions border detection via two-dimensional image analysis. *Computer Methods and Programs in Biomedicine*, *104*(3), e1–e15. https://doi.org/10.1016/j.cmpb.2010.06.016

[29]. Abbas, Q., Garcia, I. F., Emre Celebi, M., & Ahmad, W. (2013). A feature-preserving hair removal algorithm for dermoscopy images. *Skin Research and Technology*, *19*(1), e27–e36. https://doi.org/10.1111/j.1600-0846.2011.00603.x

[30]. Bansal, P., Garg, R., & Soni, P. (2022). Detection of melanoma in dermoscopic images by integrating features extracted using handcrafted and deep learning models. *Computers & Industrial Engineering*, *168*, 108060. https://doi.org/10.1016/j.cie.2022.108060

[31]. Chung, D. H., & Sapiro, G. (2000). Segmenting skin lesions with partial-differential-equations-based image processing algorithms. *IEEE Transactions on Medical Imaging*, *19*(7), 763–767. https://doi.org/10.1109/42.875204

[32]. Ganster, H., Pinz, P., Rohrer, R., Wildling, E., Binder, M., & Kittler, H. (2001). Automated melanoma recognition. *IEEE Transactions on Medical Imaging*, *20*(3), 233–239. https://doi.org/10.1109/42.918473

[33]. Lee, T., Ng, V., Gallagher, R., Coldman, A., & McLean, D. (1997). Dullrazor®: A software approach to hair removal from images. *Computers in Biology and Medicine*, *27*(6), 533–543. https://doi.org/10.1016/S0010-4825(97)00020-6

[34]. Nguyen, N. H., Lee, T. K., & Atkins, M. S. (2010). *Segmentation of light and dark hair in dermoscopic images: A hybrid approach using a universal kernel* (B. M. Dawant & D. R. Haynor, Eds.; p. 76234N). https://doi.org/10.1117/12.844572

[35]. Xie, F., Li, Y., Meng, R., & Jiang, Z. (2015). No-reference hair occlusion assessment for dermoscopy images based on distribution feature. *Computers in Biology and Medicine*, *59*, 106–115. https://doi.org/10.1016/j.compbiomed.2015.01.023

[36]. Awad, M., & Khanna, R. (2015). *Efficient learning machines*. Apress. https://doi.org/10.1007/978-1-4302-5990-9

[37]. Singhal, Y., Jain, A., Batra, S., Varshney, Y., & Rathi, M. (2018). Review of bagging and boosting classification performance on unbalanced binary classification. *2018 IEEE 8th International Advance Computing Conference (IACC)*, 338–343. https://doi.org/10.1109/IADCC.2018.8692138

[38]. Liu, H., Tian, H., Li, Y., & Zhang, L. (2015). Comparison of four Adaboost algorithm based artificial neural networks in wind speed predictions. *Energy Conversion and Management*, *92*, 67–81. https://doi.org/10.1016/j.enconman.2014.12.053

[39]. Bhavsar, H., & Panchal, M. H. (2012). A review on support vector machine for data classification. *International Journal of Advanced Research in Computer Engineering & Technology (IJARCET)*, *1*(10), 185–189.

[40]. Dreiseitl, S., & Ohno-Machado, L. (2002). Logistic regression and artificial neural network classification models: A methodology review. *Journal of Biomedical Informatics*, *35*(5–6), 352–359. https://doi.org/10.1016/S1532-0464(03)00034-0

[41]. Jiang, L., Wang, D., Cai, Z., & Yan, X. (2007). Survey of improving naive bayes for classification. In R. Alhajj, H. Gao, J. Li, X. Li, & O. R. Zaïane (Eds.), *Advanced Data Mining and Applications* (pp. 134–145). https://doi.org/10.1007/978-3-540-73871-8_14

[42]. Safavian, S. R., & Landgrebe, D. (1991). A survey of decision tree classifier methodology. *IEEE Transactions on Systems, Man, and Cybernetics*, *21*(3), 660–674. https://doi.org/10.1109/21.97458

[43]. Shafiul Azam, M., Habibullah, M., & Kabir Rana, H. (2020). Performance analysis of various machine learning approaches in stroke prediction. *International Journal of Computer Applications*, *175*(21), 11–15. https://doi.org/10.5120/ijca2020920740

[44]. Jiang, L., Cai, Z., Wang, D., & Jiang, S. (2007). Survey of improving K-nearest-neighbor for classification. *Fourth International Conference on Fuzzy Systems and Knowledge Discovery (FSKD 2007)*, 679–683. https://doi.org/10.1109/FSKD.2007.552

[45]. Nickparvar, M. (n.d.). *Brain Tumor MRI Dataset*. https://www.kaggle.com/datasets/masoudnickparvar/brain-tumor-mri-dataset/versions/1*(Accessed on 3rd March),* 2021.